

# Algorithm development and validation of CDOM properties for estuarine and continental shelf waters along the northeastern U.S. coast



Antonio Mannino<sup>a,\*</sup>, Michael G. Novak<sup>b</sup>, Stanford B. Hooker<sup>a</sup>, Kimberly Hyde<sup>c</sup>, Dirk Aurin<sup>b</sup>

<sup>a</sup> NASA Goddard Space Flight Center, Mail Code 616.1, Greenbelt, MD 20771, United States

<sup>b</sup> SSAI Inc./NASA Goddard Space Flight Center, Greenbelt, MD 20771, United States

<sup>c</sup> NOAA Northeast Fisheries Service Center, 28 Tarzwell Dr., Narragansett, RI 02882, United States

## ARTICLE INFO

### Article history:

Received 9 November 2013

Received in revised form 25 June 2014

Accepted 28 June 2014

Available online xxxx

### Keywords:

CDOM

MODIS

SeaWiFS

Chesapeake Bay

Ocean

Remote sensing

Ocean color

Continental shelf

Middle Atlantic Bight

Gulf of Maine

Georges Bank

## ABSTRACT

An extensive set of field measurements have been collected throughout the continental margin of the northeastern U.S. from 2004 to 2011 to develop and validate ocean color satellite algorithms for the retrieval of the absorption coefficient of chromophoric dissolved organic matter ( $a_{CDOM}$ ) and CDOM spectral slopes for the 275:295 nm and 300:600 nm spectral range ( $S_{275:295}$  and  $S_{300:600}$ ). Remote sensing reflectance ( $R_{rs}$ ) measurements computed from in-water radiometry profiles along with  $a_{CDOM}(\lambda)$  data are applied to develop several types of algorithms for the SeaWiFS and MODIS-Aqua ocean color satellite sensors, which involve least squares linear regression of  $a_{CDOM}(\lambda)$  with (1)  $R_{rs}$  band ratios, (2) quasi-analytical algorithm-based (QAA-based) products of total absorption coefficients, (3) multiple  $R_{rs}$  bands within a multiple linear regression (MLR) analysis, and (4) diffuse attenuation coefficient ( $K_d$ ). The relative error (mean absolute percent difference; MAPD) for the MLR retrievals of  $a_{CDOM}(275)$ ,  $a_{CDOM}(355)$ ,  $a_{CDOM}(380)$ ,  $a_{CDOM}(412)$  and  $a_{CDOM}(443)$  for our study region range from 20.4 to 23.9% for MODIS-Aqua and 27.3–30% for SeaWiFS. Because of the narrower range of CDOM spectral slope values, the MAPD for the MLR  $S_{275:295}$  and  $S_{300:600}$  algorithms are much lower ranging from 9.9% and 9.1% for SeaWiFS, respectively, and 8.7% and 9.7% for MODIS, respectively. Multi-year, seasonal and spatial MODIS-Aqua and SeaWiFS distributions of  $a_{CDOM}$ ,  $S_{275:295}$  and  $S_{300:600}$  processed with these algorithms are consistent with field measurements and the processes that impact CDOM levels along the continental shelf of the northeastern U.S. Several satellite data processing factors correlate with higher uncertainty in satellite retrievals of  $a_{CDOM}$ ,  $S_{275:295}$  and  $S_{300:600}$  within the coastal ocean, including solar zenith angle, sensor viewing angle, and atmospheric products applied for atmospheric corrections. Algorithms that include ultraviolet  $R_{rs}$  bands provide a better fit to field measurements than algorithms without the ultraviolet  $R_{rs}$  bands. This suggests that satellite sensors with ultraviolet capability could provide better retrievals of CDOM. Because of the strong correlations between CDOM parameters and DOM constituents in the coastal ocean, satellite observations of CDOM parameters can be applied to study the distributions, sources and sinks of DOM, which are relevant for understanding the carbon cycle, modeling the Earth system, and to discern how the Earth is changing.

Published by Elsevier Inc.

## 1. Introduction

Chromophoric dissolved organic matter (CDOM) represents the optically active fraction of DOM in natural waters. CDOM absorption is characterized as an exponential decrease in absorption from ultraviolet (UV) to visible wavelengths. CDOM absorption coefficients,  $a_{CDOM}(\lambda)$ , and the spectral slope coefficient ( $S$ ), a parameter that quantifies the exponential absorption decrease with increasing wavelength, have been shown to vary with type and source of CDOM (Blough & Del Vecchio, 2002; Bricaud, Morel, & Prieur, 1981). Terrestrial plant matter is considered to be the primary source of CDOM to the coastal ocean (Del Castillo, Coble, Morell, López, & Corredor, 1999; Del Vecchio &

Blough, 2004). For example, Hernes and Benner (2003) found a strong correlation between dissolved lignin phenols (compounds derived from vascular plants) and  $a_{CDOM}(350)$  within the Mississippi River plume. Such studies demonstrate that at least within the coastal ocean  $a_{CDOM}$  may be useful as a tracer of terrigenous DOM. However, biological processes such as phytoplankton growth, zooplankton grazing and microbial activity can also contribute marine-derived CDOM to continental margins and pelagic ocean (Andrew, Del Vecchio, Subramaniam, & Blough, 2013; Nelson & Siegel, 2002; Rochelle-Newall & Fisher, 2002; Steinberg, Nelson, Carlson, & Prusak, 2004). Characteristics of CDOM absorbance can be applied to trace the mixing of various water masses (e.g., Stedmon, Osburn, & Gragh, 2010). Physical processes that promote vertical mixing such as winter seasonal mixing, upwelling, and storms can introduce CDOM to the surface ocean. Deep convective mixing of the ocean by intense tropical storms such as hurricanes can also transport

\* Corresponding author. Tel.: +1 301 286 0182.

E-mail address: [antonio.mannino@nasa.gov](mailto:antonio.mannino@nasa.gov) (A. Mannino).

CDOM from depth to the surface (Hoge & Lyon, 2002). Furthermore, recent work has shown that CDOM is strongly correlated to the apparent oxygen utilization and therefore could potentially be used as a tracer of biogeochemical processes and ocean circulation in the global ocean (Nelson, Siegel, Carlson, & Swan, 2010; Swan, Siegel, Nelson, Carlson, & Nasir, 2009). Nelson and Siegel (2013) recently reviewed the distribution and dynamics of CDOM in the global ocean. CDOM can dominate the inherent light absorption at blue wavelengths in surface waters of the coastal (20–70% at 440 nm; Del Vecchio & Subramaniam, 2004; Pan, Mannino, Russ, & Hooker, 2008) and pelagic ocean (>50% at 440 nm; Siegel, Maritorena, Nelson, Hansell, & Lorenzi-Kayser, 2002). Because CDOM is ubiquitous and a dominant light absorbing constituent in the ocean, accurate retrieval of CDOM absorption is a prerequisite for applying ocean color remote sensing data to quantify other optically active ocean constituents such as chlorophyll *a* or rate processes such as phytoplankton productivity and optical properties. The impact of CDOM

absorption on photosynthetically active radiation (PAR) as well as the spectral quality of sunlight within the ocean's euphotic zone can influence primary production, primarily in regions where phytoplankton are limited by light such as in higher latitudes or in turbid waters. Seasonal vertical stratification isolates DOM at depth from sunlight, which can degrade CDOM, resulting in DOM with greater chromophoric content at depth than at the surface (Nelson & Siegel, 2002; Vodacek, Blough, DeGrandpre, Peltzer, & Nelson, 1997). The loss of CDOM from surface waters can be related to the photochemical production of dissolved inorganic carbon (e.g., Johannessen, Miller, & Cullen, 2003; Miller & Zepp, 1995).

Dissolved organic carbon (DOC) in the ocean constitutes one of the largest pools of organic carbon in the biosphere ( $700 \times 10^{15}$  g C; Field, Sarmiento, & Hales, 2007) and nearly all (>97%) of the organic carbon in the ocean (Benner, 2002). Over time, a change in the balance between production and remineralization of DOC may impact the amount of CO<sub>2</sub> in the ocean and ultimately the atmosphere. Hypothetically, an increase

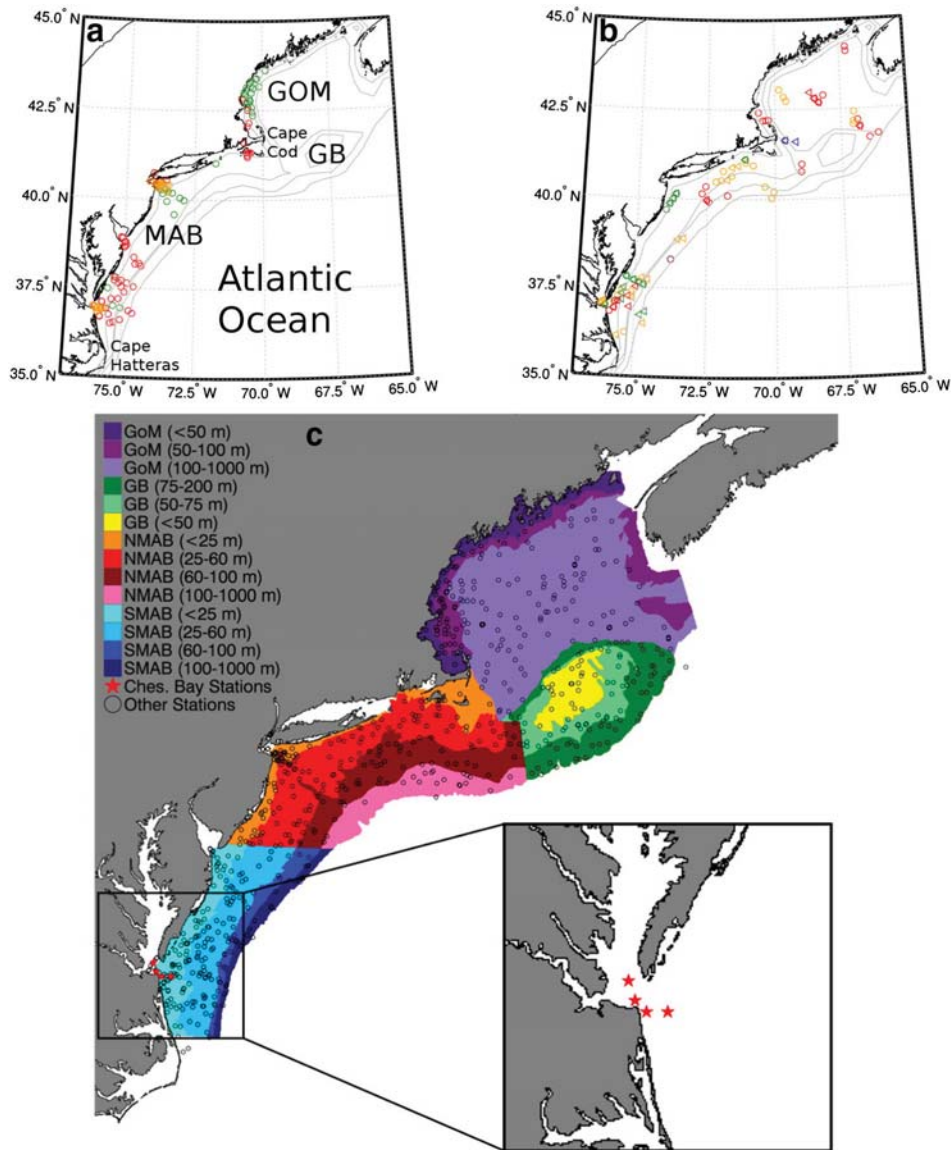


**Fig. 1.** Map of the study region and station locations sampled for (a) algorithm development, (b) validation within the coastal regions of the northwestern Atlantic Ocean, which include the Gulf of Maine (GoM), Georges Bank (GB), and Middle Atlantic Bight (MAB), and (c) time series and monthly composite comparisons with the satellite data. The symbol colors in (a) and (b) represent the season sampled: blue = winter, green = spring, red = summer, orange = fall. The symbol shapes in (b) represent the satellite sensor applied in the algorithm validation analysis: circle = MODIS-Aqua and triangle = SeaWiFS. The gray lines on (a) and (b) maps represent the approximate bathymetry contours of 20, 60, 100 and 500 m. The study regions are further subdivided into sub-regions based on bathymetry as indicated in the map legend and latitude (39° N) to distinguish the northern (NMAB) and southern MAB (SMAB) areas. The inset map shows the station locations from the lower Chesapeake Bay, mouth, plume and shelf waters for the time series comparison of field measurements and satellite retrievals of CDOM properties. (For interpretation of the references to color in this figure legend, the reader is referred to the web version of this article.)

in the oxidation of the DOC pool in the ocean (to CO<sub>2</sub>) of 1% annually would exceed the amount of CO<sub>2</sub> released from fossil fuel combustion (Hedges, 2002). Higher rates of photochemical degradation of CDOM (e.g., from increasing UV radiation to the ocean surface) and microbial respiration (related to increasing ocean temperatures) are processes that can increase the net oxidation of DOC in the ocean. Despite comprising a relatively small fraction of DOM, CDOM strongly correlates with DOC in rivers, river plumes, estuaries and continental margins (e.g., Del Castillo et al., 1999; Ferrari, Dowell, Grossi, & Targa, 1996; Mannino, Russ, & Hooker, 2008; Spencer, Butler, & Aiken, 2012; Stedmon, Markager, & Kaas, 2000; Vodacek et al., 1997), but not in pelagic ocean waters (Nelson & Siegel, 2002). The strong relationships between CDOM absorption and DOM in coastal waters provide a means to quantify DOC as well as sources and sinks of DOM from satellite retrievals of CDOM absorption.

Numerous bio-optical algorithms have been developed to retrieve CDOM absorption or closely related products from ocean color satellite observations including SeaWiFS (Sea-viewing Wide Field-of-view

Sensor), MODIS (MODerate resolution Imaging Spectroradiometer) on the Aqua satellite, and MERIS (MEDIUM-spectral Resolution Imaging Spectrometer). Many of these inversion models estimate the absorption coefficient of CDOM and detrital (non-pigmented) particles as a single parameter ( $a_{CDM}$ ), because CDOM and detritus have similar spectral responses in the visible spectrum (Bricaud, Ciotti, & Gentili, 2012; Carder, Chen, Lee, Hawes, & Kamykowski, 1999; Doerffer & Schiller, 2007; Hoge, Wright, Lyon, Swift, & Yungel, 2001; Lee, Arnone, Hu, Werdell, & Lubac, 2010; Lee, Carder, & Arnone, 2002; Maritorena, Siegel, & Peterson, 2002; Siegel, Maritorena, Nelson, & Behrenfeld, 2005; Siegel, Maritorena, Nelson, Behrenfeld, & McClain, 2005; Tilstone et al., 2012; Werdell et al., 2013). In oligotrophic ocean waters such as the Sargasso Sea, non-pigmented particles account for only ~12% of CDM absorption (Siegel et al., 2002). Recent work in coastal ocean waters indicates that non-pigmented particles account for <20% of total light absorption at 443 nm along the U.S. Mid-Atlantic coast (Pan et al., 2008). The various inversion models apply remote sensing reflectance ( $R_{rs}$ ) for several wavelength bands to simultaneously derive multiple parameters

**Table 1**

List of sampling cruises and measurements collected for the naperian absorption coefficient of colored dissolved organic matter ( $a_{CDOM}$ ) algorithm development or validation.

Region	Cruise	Dates	Measurements	Stations <sup>a</sup>	
				CDOM	AOPs
Lower CB <sup>b</sup>	CBM01	5 May 2004	CDOM <sup>c</sup>	2, 0, 0	
Lower CB	CBM02	5 July 2004	CDOM	4, 0, 0	
Lower CB	CBM03	1 September 2004	CDOM	4, 0, 1	
Lower CB	CBM04	15 October 2004	CDOM	4, 0, 0	
Lower CB	CBM05	15 November 2004	CDOM	4, 0, 2	
Lower CB	CBM06	10 January 2005	CDOM	4, 0, 0	
Lower CB	CBM07	26 May 2005	CDOM	3, 0, 1	
Lower CB	CBM08	21 June 2005	CDOM	3, 0, 0	
Lower CB	CBM09	19 August 2005	CDOM	4, 0, 0	
Lower CB	CBM10	23 September 2005	CDOM	4, 0, 2	
Lower CB	CBM11	30 January 2006	CDOM	3, 0, 0	
Lower CB	CBM12	12 April 2006	CDOM	4, 0, 0	
CB Mouth & Plume	D01	27 May 2005	CDOM & AOPs <sup>d</sup>	4, 2, 1	4, 2, 1
CB Mouth & Plume	D02	3 November 2005	CDOM & AOPs	6, 6, 0	6, 6, 5
CB Mouth & Plume	D03	6 September 2006	CDOM & AOPs	5, 2, 0	2, 2, 0
CB Mouth & Plume	D04	28 November 2006	CDOM & AOPs	6, 3, 0	3, 3, 0
CB Mouth & Plume	PL6	19 March 2007	CDOM	4, 0, 2	
CB Mouth & Plume	COI1	23 April 2007	CDOM	4, 0, 2	
CB Mouth & Plume	COI2	3 July 2007	CDOM	4, 0, 2	
CB Mouth & Plume	COI3	16 August 2007	CDOM	4, 0, 0	
Southern MAB <sup>e</sup>	B01	30 March–1 April 2005	CDOM & AOPs	14, 5, 0	5, 5, 0
Southern MAB	B02	26–30 July 2005	CDOM & AOPs	29, 18, 0	18, 18, 4
Southern MAB	B03	9–12 May 2006	CDOM	26, 0, 4	
Southern MAB	B04	2–6 July 2006	CDOM & AOPs	31, 30, 0	30, 30, 3
Southern MAB	B05	31 Oct.–2 Nov. 2006	CDOM	16, 0, 1	
GoM <sup>f</sup>	BIOD01	26–30 April 2007	CDOM & AOPs	14, 9, 0	9, 9, 0
GoM	BIOD02	26–28 May 2007	CDOM & AOPs	17, 14, 0	14, 14, 3
GoM & MVCO <sup>g</sup>	BIOD03	6–8 June 2007	CDOM & AOPs	13, 11, 0	11, 11, 0
NYB <sup>h</sup>	OCV1	5–9 May 2007	CDOM & AOPs	20, 20, 0	20, 20, 8
NYB	OCV2	10–14 Nov. 2007	CDOM & AOPs	22, 16, 0	16, 16, 4
NYB	OCV3	21–23 July 2008	CDOM & AOPs	8, 8, 0	8, 8, 0
NYB	OCV5	19–21 May 2009	CDOM & AOPs	11, 11, 0	11, 11, 3
MAB, GoM, GB <sup>i</sup>	CV1	17–28 August 2009	CDOM	51, 0, 10	
MAB, GoM, GB	CV2	3–20 Nov. 2009	CDOM	69, 0, 19	
MAB, GoM, GB	CV3	1–17 February 2010	CDOM	45, 0, 4	
MAB, GoM, GB	CV4	26 May–9 June 2010	CDOM	79, 0, 14	
MAB, GoM, GB	CV5	6–21 Nov. 2010	CDOM	69, 0, 10	
MAB, GoM, GB	CV6	2–21 June 2011	CDOM	93, 0, 9	

<sup>a</sup> Number of stations measured or applied for CDOM algorithm development and validation (n, n, n), respectively and number of stations where AOP profiles were collected, used for CDOM algorithm development, and for validation of satellite remote sensing reflectance (n, n, n). For validation, only stations meeting the validation criteria for either MODIS-Aqua or SeaWiFS are listed. Blank cells indicate that no measurements were collected or applied. For a sub-set of stations, a second set of CDOM samples and series of AOP profiles were collected or conducted within approximately one hour of the first set of measurements.

<sup>b</sup> Lower CB – Old Dominion University's Chesapeake Bay mouth hydrography transect north of the Chesapeake Bay bridge and tunnel system.

<sup>c</sup> CDOM – spectral absorption coefficients of colored dissolved organic matter.

<sup>d</sup> AOPs – apparent optical properties including spectral water-leaving radiances, remote sensing reflectances and light attenuation coefficients.

<sup>e</sup> Southern MAB – Delaware Bay and Chesapeake Bay mouths, plume and adjacent continental margin of the southern Middle Atlantic Bight (MAB).

<sup>f</sup> GoM – Gulf of Maine.

<sup>g</sup> MVCO – area surrounding the Martha's Vineyard Coastal Observatory (MVCO) south of Cape Cod, Massachusetts.

<sup>h</sup> NYB – lower Hudson River, Hudson–Raritan Bay and plume and adjacent continental margin of the New York Bight (NYB).

<sup>i</sup> GB – Georges Bank.

including  $a_{CDM}$ ,  $a_{ph}$  (phytoplankton absorption coefficient) or chlorophyll  $a$  (Chl), and the particulate backscatter coefficient. Satellite products are also derived through empirical methods that relate  $a_{CDOM}$  to  $R_{rs}$  band-ratios of various ocean color bands (e.g., Kahru & Mitchell, 2001; Shanmugam, 2011). Various  $R_{rs}$  band-ratio algorithms [ $R_{rs}(\lambda_1)/R_{rs}(\lambda_2)$ ] have been developed to retrieve  $a_{CDOM}$  within coastal regions such as  $R_{rs}(443\text{ nm})/R_{rs}(555\text{ nm})$  (D'Sa & Miller, 2003; D'Sa, Miller, & Del Castillo, 2006; Del Castillo & Miller, 2008; Johannessen et al., 2003; Kahru & Mitchell, 2001; Mannino et al., 2008; Naik, D'Sa, Grippo, Condrey, & Fleeger, 2011) and global ocean (Shanmugam, 2011; Tiwari & Shanmugam, 2011). Retrieval of  $a_{CDM}$  using inversion algorithms yields reasonable results in open ocean regions (Siegel, Maritorena, Nelson, Behrenfeld, & McClain, 2005; Siegel et al., 2002). However, such algorithms typically do not work well in coastal waters due to the optical complexity of turbid coastal waters (high levels of CDOM, colored detrital

particles, and phytoplankton; e.g., Aurin & Dierssen, 2012) as well as simplified parameterization (e.g., single  $S$  to represent marine waters globally; Maritorena et al., 2002; Magnuson, Harding, Mallonee, & Adolf, 2004; Morel & Gentili, 2009). Recent approaches have attempted to separate  $a_{CDOM}$  from  $a_{CDM}$  (Dong, Shang, & Lee, 2013; Matsuoka, Hooker, Bricaud, Gentili, & Babin, 2013; Tilstone et al., 2012) and to derive the CDOM spectral slope in various spectral regions (Fichot et al., 2013; Mannino et al., 2008). Despite the many algorithms developed to retrieve  $a_{CDOM}$  and  $a_{CDM}$  from satellite data only a few have undergone rigorous validation involving direct comparison of field measurements with coincident satellite data. The primary limitation to rigorous validation is the lack of sufficient data of coincident field measurements and satellite observations that are independent from the data used to develop the algorithm.

Accurate retrievals of  $a_{CDOM}(\lambda)$  are needed to improve satellite estimates of Chl. The intense and spectrally coincident absorption by CDOM

**Table 2**  
Spatial and temporal range of in situ CDOM measurements. Mean +/- sd.

Sub-region	Season	$a_{CDOM355}$		$a_{CDOM412}$		$S_{275:295}$		$S_{300:600}$		n	
		Mean	±sd	Mean	±sd	Mean	±sd	Mean	±sd		
Gulf of Maine <50 m	Spring	1.033	0.750	0.393	0.295	0.0213	0.0025	0.0180	0.0008	6	
	Summer	1.470	0.202	0.574	0.083	0.0182	0.0009	0.0169	0.0004	11	
	50–100 m	Winter	1.437	0.554	0.562	0.221	0.0185	0.0016	0.0170	0.0005	14
		Spring	0.419	0.049	0.171	0.023	0.0236	0.0010	0.0176	0.0010	8
		Summer	0.563	0.155	0.226	0.063	0.0220	0.0016	0.0175	0.0005	6
	100–1000 m	Fall	0.632	0.178	0.240	0.064	0.0233	0.0017	0.0182	0.0011	18
		Winter	0.571	0.376	0.219	0.142	0.0237	0.0034	0.0185	0.0008	6
		Spring	0.332	0.080	0.131	0.034	0.0253	0.0014	0.0186	0.0010	12
	Georges Bank <50 m	Summer	0.302	0.045	0.121	0.018	0.0264	0.0009	0.0191	0.0004	25
Fall		0.384	0.107	0.146	0.041	0.0264	0.0016	0.0192	0.0010	75	
Winter		0.261	0.019	0.109	0.007	0.0261	0.0005	0.0189	0.0003	5	
50–75 m	Summer	0.369	0.065	0.159	0.033	0.0256	0.0016	0.0179	0.0009	14	
	Fall	0.326	0.026	0.136	0.018	0.0256	0.0008	0.0187	0.0006	3	
	Winter	0.279	0.021	0.118	0.007	0.0259	0.0002	0.0185	0.0004	4	
75–200 m	Summer	0.304	0.040	0.122	0.020	0.0275	0.0011	0.0191	0.0008	28	
	Fall	0.319	0.038	0.132	0.018	0.0261	0.0006	0.0186	0.0006	6	
	Winter	0.265	0.061	0.105	0.021	0.0266	0.0012	0.0189	0.0007	10	
Northern MAB <25 m	Summer	0.283	0.057	0.110	0.026	0.0283	0.0018	0.0198	0.0011	23	
	Fall	0.240	0.099	0.098	0.040	0.0296	0.0047	0.0194	0.0008	16	
	Winter	0.477	0.103	0.199	0.036	0.0235	0.0012	0.0176	0.0004	4	
25–60 m	Spring	1.099	0.410	0.429	0.164	0.0206	0.0028	0.0180	0.0011	14	
	Summer	0.650	0.197	0.260	0.088	0.0226	0.0028	0.0183	0.0008	20	
	Fall	0.537	0.164	0.218	0.058	0.0242	0.0018	0.0182	0.0004	15	
60–100 m	Winter	0.358	0.081	0.151	0.032	0.0253	0.0015	0.0180	0.0005	14	
	Spring	0.557	0.263	0.214	0.105	0.0245	0.0029	0.0194	0.0013	24	
	Summer	0.489	0.170	0.186	0.067	0.0256	0.0023	0.0192	0.0012	35	
100–1000 m	Fall	0.405	0.081	0.167	0.032	0.0255	0.0011	0.0183	0.0004	35	
	Winter	0.239	0.068	0.105	0.031	0.0276	0.0019	0.0183	0.0007	5	
	Spring	0.284	0.034	0.103	0.015	0.0284	0.0009	0.0211	0.0007	4	
Southern MAB <25 m	Summer	0.285	0.088	0.106	0.036	0.0292	0.0022	0.0207	0.0015	23	
	Fall	0.312	0.052	0.129	0.024	0.0266	0.0013	0.0186	0.0006	15	
	Winter	0.190	0.083	0.080	0.034	0.0291	0.0036	0.0192	0.0014	3	
25–60 m	Summer	0.203	0.033	0.074	0.015	0.0315	0.0020	0.0209	0.0011	12	
	Fall	0.247	0.052	0.103	0.023	0.0282	0.0012	0.0188	0.0005	6	
	Winter	0.493	0.077	0.202	0.031	0.0236	0.0013	0.0179	0.0005	7	
60–100 m	Spring	0.785	0.373	0.296	0.135	0.0236	0.0021	0.0191	0.0009	40	
	Summer	0.786	0.312	0.301	0.129	0.0242	0.0028	0.0191	0.0015	60	
	Fall	0.908	0.453	0.342	0.159	0.0234	0.0016	0.0187	0.0007	44	
100–1000 m	Winter	0.267	0.041	0.121	0.016	0.0265	0.0001	0.0173	0.0004	3	
	Spring	0.331	0.060	0.127	0.025	0.0273	0.0015	0.0200	0.0011	20	
	Summer	0.376	0.132	0.135	0.055	0.0286	0.0024	0.0213	0.0016	55	
25–60 m	Fall	0.319	0.054	0.127	0.024	0.0276	0.0012	0.0192	0.0012	19	
	Winter	0.156	0.061	0.071	0.027	0.0306	0.0021	0.0178	0.0010	3	
	Spring	0.263	0.038	0.102	0.016	0.0284	0.0014	0.0199	0.0010	7	
60–100 m	Summer	0.279	0.142	0.106	0.055	0.0311	0.0026	0.0209	0.0019	6	
	Fall	0.227	0.023	0.089	0.015	0.0289	0.0006	0.0195	0.0009	3	
	Winter	0.160	0.037	0.072	0.018	0.0298	0.0023	0.0185	0.0011	5	
100–1000 m	Spring	0.178	0.048	0.071	0.015	0.0306	0.0027	0.0194	0.0011	2	
	Summer	0.195	0.124	0.070	0.051	0.0338	0.0036	0.0223	0.0030	8	
	Fall	0.230	0.110	0.084	0.039	0.0305	0.0025	0.0204	0.0006	3	

and Chl within the blue spectrum, which includes the Chl absorption peak near 443 nm, reduces the accuracy of satellite retrievals of Chl, especially for the heritage band-ratio algorithms (Carder et al., 1991; Siegel et al., 2013; Siegel, Maritorena, Nelson, & Behrenfeld, 2005; Siegel, Maritorena, Nelson, Behrenfeld, & McClain, 2005). Indeed, concurrent changes in satellite CDOM and Chl using the standard Chl product (O'Reilly et al., 2000) provides false global-scale trends in Chl (Brown, Huot, Werdell, Gentili, & Claustre, 2008; Siegel et al., 2013). The capability to accurately retrieve  $a_{CDOM}(\lambda)$  provides the potential for improving satellite retrievals of Chl.

Recent findings demonstrating the utility of the CDOM spectral slope at various wavelength ranges (Fichot & Benner, 2012; Helms et al., 2008; Loisele et al., 2009) have prompted greater interest in satellite retrieval of  $S$ . For example, the ratio of  $S_{275:295}$  and  $S_{350:400}$  is a very good indicator of DOM photochemical versus microbial degradation processes (Helms et al., 2008). Satellite retrieval of  $S_{300:600}$  and  $a_{CDOM}$  at a single wavelength within that spectral range allows computation of  $a_{CDOM}$  at any wavelength within the 300:600 nm spectral ranges using the CDOM spectral slope equation (Bricaud et al., 1981). Furthermore, strong correlations between  $S_{275:295}$  and lignin phenol yields (Fichot & Benner, 2012) can be used to derive lignin phenol yields from satellite retrievals of  $S_{275:295}$  (Fichot et al., 2013) for subsequent estimation of vascular plant contributions to DOM in surface ocean waters.

Ocean color satellite retrievals of  $a_{CDOM}$  and  $S$  have many potential applications. Thus, the objectives of our work are (1) to develop bio-optical algorithms using field data from our study region within the northeast U.S. continental shelf, (2) validate these algorithms for SeaWiFS and MODIS-Aqua sensors, (3) examine what factors add significant uncertainty in satellite retrievals of  $a_{CDOM}$  and  $S$ , (4) describe the distributions of  $a_{CDOM}$  and  $S$  from SeaWiFS and MODIS retrievals, and (5) evaluate whether radiometric measurements in the UV can improve the fidelity of  $a_{CDOM}$  and  $S$  algorithms. The results presented here are drawn from field sampling activities supported through multiple research grants in order to accumulate sufficient quantities of algorithm-independent coincident observations of satellite data and field observations.

## 2. Methods

### 2.1. Study area

Measurements for this study were collected throughout the lower estuaries and continental margin of the northeastern U.S. between Cape Hatteras, North Carolina and southern Nova Scotia, Canada, which comprises the northeast U.S. continental shelf Large Marine Ecosystem (NES LME). For the purposes of this study and on the basis

of ocean circulation, geography and bathymetry, the continental margin of the northeastern U.S. is subdivided into three regions (Fig. 1). The Middle Atlantic Bight (MAB) extends from Cape Hatteras, North Carolina to Cape Cod, Massachusetts. The Gulf of Maine (GoM) extends from Cape Cod to southern Nova Scotia, Canada. Georges Bank (GB) consists of the region to the southeast, east and northeast of Cape Cod (Fig. 1). The MAB is further sub-divided into the northern and southern MAB as shown in Fig. 1c.

### 2.2. Field sampling

Multiple research cruises were conducted in the southern MAB from March 2005 to August 2007, lower Chesapeake Bay from May 2004 to August 2007, Gulf of Maine from April to June 2007, New York Bight (Hudson–Raritan Bay and adjacent coastal ocean) from May 2007 to May 2009, and across all continental shelf regions from August 2009 to June 2011 (Fig. 1; Table 1). Seawater samples were collected with Go-Flo bottles at multiple depths per station. Additional samples were collected via peristaltic pumping from ~0.5 m to 1 m depth to obtain coincident samples with in-water radiometry profiles as well as through the ships' clean seawater flow-through systems.

### 2.3. Sample processing, storage, and analysis

Seawater samples for measurement of CDOM absorbance spectra are collected, filtered, stored and analyzed as described in Mannino et al. (2008) and described here in abridged form. Samples are filtered through combusted Whatman GF/F glass fiber filters by gentle vacuum and collected directly into glass storage bottles. Samples are kept on ice for transport or in a refrigerator (4 to 8 °C) for longer-term storage. For analysis, CDOM samples are warmed to room temperature and filtered through either 0.2 µm Gelman Supor (polyethersulfone) filters or Whatman Nuclepore (polycarbonate) filters, which are pre-rinsed with ultrapure water (Milli-Q) and sample water. CDOM absorbance spectra are measured on a double-beam Cary 100 Ultraviolet–Visible scanning spectrophotometer using Suprasil quartz cylindrical cells of 100 mm pathlength with ultraviolet oxidized Milli-Q water as the blank and reference (Mannino et al., 2008; Mitchell, Kahru, Wieland, & Stramska, 2003). Scan settings for the spectrophotometer are as follows: 4 nm slit width, 250–800 nm wavelength range, 1 nm data interval, and 100 nm min<sup>-1</sup> scan rate. The instrument noise for reference baseline spectral scans of air-to-air and Milli-Q water is evaluated daily to be within ±0.0005 absorbance units. Typically, raw absorbance measurements are corrected with field filtration blanks of UV-oxidized Milli-Q and a null point value (Mitchell et al., 2000, 2003). Since the absorbance of filtration blanks and null point values are typically within the level of instrument noise, corrections are applied on a

**Table 3**

Coefficients and goodness of fit parameters for band-ratio bio-optical  $a_{CDOM}$  algorithms developed from field observations of  $a_{CDOM}(\lambda)$  and remote sensing reflectance ( $R_{rs}(\lambda)$ ).  $R^2$  is the non-linear regression coefficient.  $Sy.x$  represents the standard deviation of the residuals reported in units of the Y-axis variable, and  $n$  is the sample size. The minimum band ratio represents the threshold  $R_{rs}$  band ratio value at which the algorithm loses sensitivity below this value (at high  $a_{CDOM}$  values).

Exponential one-phase decay equation	$a_{CDOM275}$	$a_{CDOM355}$	$a_{CDOM380}$	$a_{CDOM412}$	$a_{CDOM443}$
$X = \ln[(Y - B_0) / B_2] / -B_1$	$B_0 = 0.2792$	0.2652	0.2676	0.2675	0.2678
$Y = R_{rs}(412) / R_{rs}(547)$	$B_1 = 1.582$	5.534	8.484	13.74	23.28
$X = a_{CDOM}(\lambda)$	$B_2 = 21.95$	4.337	4.054	3.619	3.406
$R^2$	0.880	0.934	0.944	0.947	0.928
$Sy.x$	0.099	0.0838	0.077	0.0757	0.082
$n$	140	152	152	153	150
Minimum band ratio	0.31	0.295	0.295	0.295	0.295
$X = \ln[(Y - B_0) / B_2] / -B_1$	$B_0 = 0.9686$	0.7723	0.685	0.7074	0.7857
$Y = R_{rs}(412) / R_{rs}(670)$	$B_1 = 2.302$	7.794	9.522	15.86	31.79
$X = a_{CDOM}(\lambda)$	$B_2 = 958.4$	92.44	47.35	43.85	56.59
$R^2$	0.844	0.943	0.954	0.946	0.936
$Sy.x$	0.986	0.817	0.692	0.605	0.749
$n$	138	146	140	137	144
Minimum band ratio	1.29	1.1	1.1	1.1	1.1

limited set of samples. For the most recent sample collections (August 2009 to the present), a null point correction value is applied to all samples from the mean optical density within 695–700 nm. The naperian CDOM absorption coefficients are calculated from the following equation:

$$a_{CDOM}(\lambda) = 2.303 A(\lambda)/L \quad (1)$$

where  $A(\lambda)$  is the absorbance of filtered seawater at a specific wavelength measured across pathlength  $L$  in meters. The CDOM spectral slope coefficients ( $S$ ) are determined by fitting a single-exponential non-linear curve on multiple spectral ranges for each  $a_{CDOM}$  wavelength range (275–295 and 300–600 nm;  $S_{275:295}$  and  $S_{300:600}$ ) using the following expression:

$$a(\lambda) = a(\lambda_0)e^{-S(\lambda - \lambda_0)} \quad (2)$$

where  $a(\lambda)$  and  $a(\lambda_0)$  represent the absorption coefficients at wavelength  $\lambda$  and reference wavelength  $\lambda_0$ .

#### 2.4. Apparent optical properties (AOP)

Radiometry profiles were collected using either the Biospherical Profiler (BioPRO) or the Submersible Biospherical Optical Profiling System (SuBOPS). BioPRO is a compact rocket-shaped device, whereas the SuBOPS device uses a small kite-shaped backplane (Hooker, Lind, Morrow, & Brown, 2010). Both instruments were floated away to avoid deployment-platform perturbations and use the same 19-channel sensors spanning 320–875 nm with approximately 10 decades of dynamic range and a 12 Hz sampling rate. The adjustable buoyancy permits stable descents with vertical tilts to within 5°. The SuBOPS uses a hydrobaric buoyancy system and adjustable sensor orientation to achieve stable descents as slow as 5 cm s<sup>-1</sup> with vertical tilts to within 2.5°. SuBOPS can achieve 1 cm (or less) vertical resolution in near-surface waters, because the compressible bladders in the hydrobaric buoyancy system allow the profiler to loiter close to the surface before reaching terminal velocity (usually set to 3–5 m). Both instruments possess 19 micro-radiometers each with 10 nm-wide bands centered at the following wavelengths: 320, 340, 380, 395, 412, 443, 465, 490, 510, 532, 555, 560, 625, 665, 670, 683, 710, 780, and 860 or 870 nm.

The significance of acquiring useful data close to the sea surface is expressed directly in the processing scheme used to derive data products from the light measurements. The processor used here is based on a well-established methodology (Smith & Baker, 1984) that was evaluated in an international round robin (Hooker et al., 2001) and shown to be capable of agreement at the 1% level when the processing options were as similar as possible. Complete details for the terms and dependencies are available in the Ocean Optics Protocols (hereafter, the Protocols), which initially adhered to the Joint Global Ocean Flux Study (JGOFS) sampling procedures (Joint Global Ocean Flux Study, 1991) and defined the standards for NASA calibration and validation activities (Mueller & Austin, 1992). Over time, the Protocols were initially revised (Mueller & Austin, 1995), and then updated annually (Mueller, 2000, 2002, 2003).

The Protocols are detailed, so only a brief overview for obtaining data products from vertical profiles of upwelling radiance ( $L_u$ ) plus downward irradiance ( $E_d$ , respectively) are presented here. In-water radiometric quantities in physical units,  $\beta$  (i.e.,  $L_u$  or  $E_d$ ), are normalized with respect to simultaneous measurements of the global solar irradiance,  $E_d(0+, \lambda, t)$ , with  $t$  explicitly expressing the time dependence, according to

$$\beta(z, \lambda, t_0) = \beta(z, \lambda, t)E_d(0+, \lambda, t_0)/E_d(0+, z, t) \quad (3)$$

where  $\beta(z, \lambda, t_0)$  identifies the radiometric parameters as they would have been recorded at all depths  $z$  at the same time  $t_0$ , and  $t_0$  is generally chosen to coincide with the start of data acquisition. For simplicity, the

variable  $t$  is omitted in the following text. In addition, any data collected when the vertical tilt of the profiler exceeds 5° are excluded from the ensuing analysis.

After normalization and tilt filtering, a near-surface portion of  $E_d(z, \lambda)$  centered at  $z_0$  and having homogeneous optical properties (verified with temperature and attenuation parameters) extending from  $z_1 = z_0 + \Delta z$  and  $z_2 = z_0 - \Delta z$  is established separately for the blue-green and red wavelengths; the ultraviolet (UV) is included

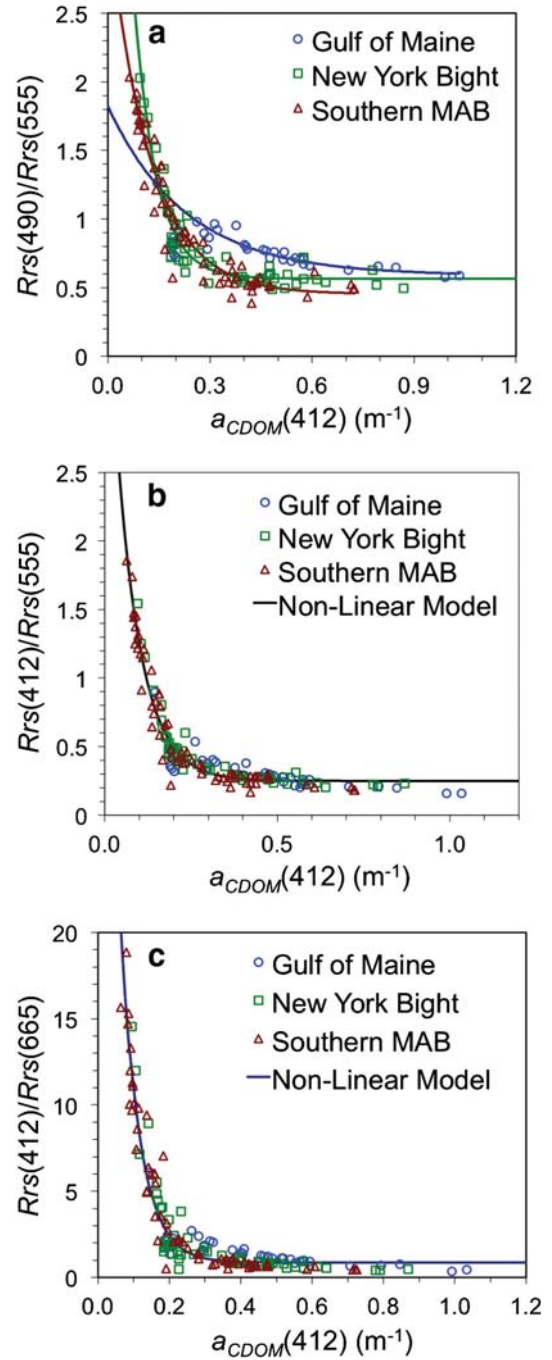


**Fig. 2.** Representation of band ratio algorithms from field measurements of the absorption coefficient of colored dissolved organic matter [ $a_{CDOM}(412)$ ] and remote sensing reflectance ( $R_{rs}$ ) band ratios (a)  $R_{rs}(490)/R_{rs}(555)$ , (b)  $R_{rs}(412)/R_{rs}(555)$ , and (c)  $R_{rs}(412)/R_{rs}(665)$  for three coastal regions along the northeastern U.S., which include the Gulf of Maine, New York Bight (region between northern New Jersey and Long Island, New York) and Southern Middle Atlantic Bight (SMAB). The symbols represent the field observations and the lines represent the predicted values produced from the non-linear model derived for each region or all regions combined.

in the interval most similar to the UV attenuation scales. Both intervals begin at the same shallowest depth, but the blue-green interval is allowed to extend deeper if the linearity in  $\ln[L_u(z, \lambda)]$ , as determined statistically, is thereby improved. The negative value of the slope of the regression yields the diffuse attenuation coefficient,  $K_d(\lambda)$ , which is used to extrapolate the fitted portion of the  $E_d$  profile through the near-surface layer to null depth,  $z = 0^-$ .

Fluctuations caused by surface waves and so-called lens effects prevent accurate measurements of  $E_d(\lambda)$  close to the surface. A value just below the surface (at null depth  $z = 0^-$ ) can be compared to that measured contemporaneously above the surface (at  $z = 0^+$ ) with a separate solar reference using

$$E_d(0^-, \lambda) = 0.97E_d(0^+, \lambda), \tag{4}$$

where the constant 0.97 represents the applicable air–sea transmittance, Fresnel reflectances, and the irradiance reflectance, and is determined to an accuracy better than 1% for solar elevations above 30° and low-to-moderate wind speeds (Antoine, Hooker, Bélanger, Matsuoka, & Babin, 2013). The distribution of  $E_d$  measurements at any depth  $z$  influenced by wave focusing effects does not follow a Gaussian distribution, so linear fitting of  $E_d$  in a near-surface layer is poorly constrained, especially if the number of samples is small. The application of Eq. (4) to the fitting process establishes a boundary condition or constraint for the fit.

The appropriateness of the  $E_d$  extrapolation interval, initially established by  $z_1$  and  $z_2$ , is evaluated by determining if Eq. (4) is satisfied to within approximately the uncertainty of the calibrations (a few percent); if not,  $z_1$  and  $z_2$  are re-determined while keeping the selected depths within the shallowest homogeneous layer possible until the disagreement is minimized (usually to within 5%). The linear decay of  $\ln[\beta(z, \lambda)]$ , for all light parameters in the chosen near-surface layer are then evaluated, and if linearity is acceptable, the entire process is repeated on a cast-by-cast basis. Subsurface primary quantities at null depth,  $\beta(0^-, \lambda)$ , are obtained from the slope and intercept given by the least-squares linear regression of  $\ln[\beta(z, \lambda)]$  versus  $z$  within the extrapolation interval specified by  $z_1$  and  $z_2$ .

The water-leaving radiance is obtained directly from

$$L_W(\lambda) = 0.54L_u(0^-, \lambda) \tag{5}$$

where the constant 0.54 accurately accounts for the partial reflection and transmission of the upwelled radiance through the sea surface, as confirmed by Mobley (1999). To account for the aforementioned dependence of  $L_W$  on the solar flux, which is a function of atmospheric conditions and time of day,  $L_W$  is normalized by the (average) global

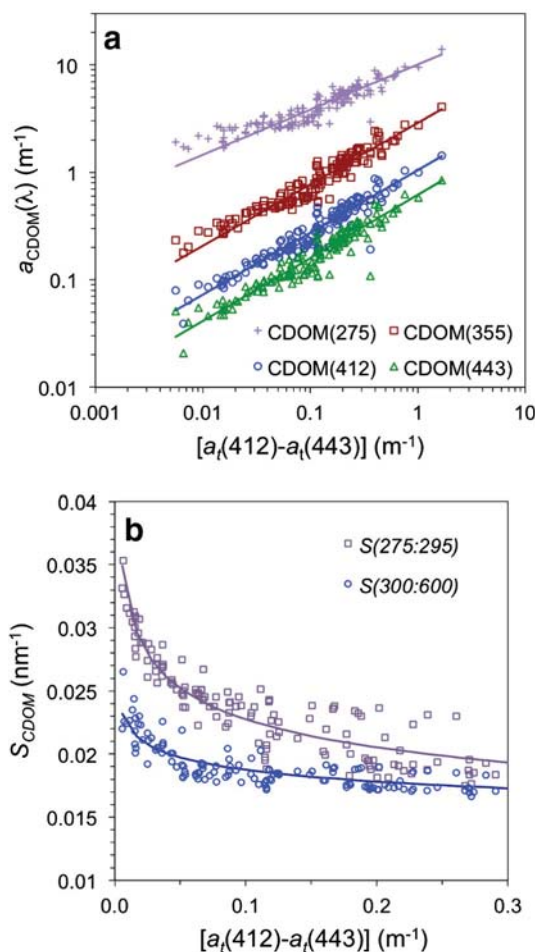


Fig. 3. Field measurement-based relationships of the total absorption coefficient [ $a_t$ ] difference of  $a_t(412)$  and  $a_t(443)$  with (a)  $a_{CDOM}(275)$ ,  $a_{CDOM}(355)$ ,  $a_{CDOM}(412)$  and  $a_{CDOM}(443)$  and (b) CDOM spectral slope for two wavelength regions  $S_{275:295}$  and  $S_{300:600}$ .  $a_t(412)$  and  $a_t(443)$  were computed from in situ  $R_{rs}$  data using version 5 of the Quasi-Analytical Algorithm (QAA) from Lee et al., 2010, 2002. The symbols represent the field observations and the lines represent the predicted values produced from the non-linear models.

solar irradiance measured during the time interval corresponding to  $z_1$  and  $z_2$ :

$$R_{rs}(\lambda) = L_W(\lambda)/E_d(0^+, \lambda), \tag{6}$$

where  $R_{rs}$  is the remote sensing reflectance.

Table 4

Coefficients and goodness of fit parameters for bio-optical CDOM algorithms developed from field observations of  $a_{CDOM}(\lambda)$  and Quasi Analytical Algorithm (QAA) total absorption coefficient [ $a_t(\lambda)$ ] derived from remote sensing reflectance.

Equation	$a_{CDOM275}$	$a_{CDOM355}$	$a_{CDOM380}$	$a_{CDOM412}$	$a_{CDOM443}$	$S_{275:295}$	$S_{300:600}$
<i>QAA product-based</i>							
$Y = A * X^B$	A = 10.08 B = 0.4207	2.671 0.575	1.771 0.5829	1.048 0.5797	0.617 0.587	0.0158 −0.0737	0.0162 −0.1483
$X = a_t(412) - a_t(443)$							
$Y = a_{CDOM}(\lambda)$ or $S_{CDOM}(\lambda_1:\lambda_2)$							
$R^2$	0.884	0.927	0.929	0.934	0.928	0.746	0.881
Sy.x	0.664	0.1467	0.0962	0.0547	0.0339	0.00088	0.00144
n	150	148	148	148	148	150	150
$Y = A * X^B$	A = B =	1.236 0.600	0.813 0.616	0.499 0.646	0.286 0.648		
$X = a_t(412)$							
$Y = a_{CDOM}(\lambda)$							
$R^2$		0.805	0.811	0.838	0.826		
Sy.x		0.198	0.130	0.0754	0.0458		
n		144	144	145	145		

2.5. CDOM algorithm development

Spectral remote sensing reflectance derived from in situ radiometry profiles and  $a_{CDOM}(\lambda)$  were applied to develop multi-regional satellite algorithms to retrieve  $a_{CDOM}$  and CDOM spectral slopes for the NES LME region. The station locations for measurements applied to derive algorithms of CDOM properties are shown in Fig. 1a (see Table 1 for additional details). A least squares approach was applied to field measurements to develop and evaluate multiple non-linear regression curve-fitting solutions as well as multiple linear regression analysis to retrieve  $a_{CDOM}(\lambda)$  from AOP-derived products ( $R_{rs}$ ,  $K_d$ , inherent optical properties (IOP)). We regressed  $a_{CDOM}(\lambda)$  and  $S$  with  $R_{rs}$  band ratios,  $K_d$ , and IOP products to deduce algorithms that are optimal for our study region. A series of absorption and backscatter products were derived from  $R_{rs}$  data using version 5 of the Quasi-Analytical Algorithm (QAA v5; Lee et al., 2010, 2002). The QAA products applied for algorithm development include the total absorption coefficient ( $a_t$ ) at 412 nm and the difference in  $a_t(412)$  and  $a_t(443)$ , because the total absorption and backscatter products are considered to be the most robust products as opposed to the constituent products of phytoplankton ( $a_{ph}$ ) and colored detritus absorption coefficients ( $a_{CDM}$ ). The QAA-derived [ $a_t(412) - a_t(443)$ ] was applied to reduce the contribution of phytoplankton absorption, because phytoplankton absorption is much higher at 443 nm than 412 nm, and this formulation would thus accentuate the CDOM absorption. The evaluation of the algorithm relationship is based on least squares statistics including the regression coefficient ( $R^2$ ), the standard deviation of the data points from the non-linear regression curve fit (Sy,x) or the mean square error (MSE) and visual inspection of the in situ data and the modeled curve fit. Non-linear regression curve fitting and single linear regression analyses were conducted using Prism 5.0b (GraphPad Software, Inc.). The statistical software package SYSTAT 13 (Systat Software) was applied for the multiple linear regression analysis.

2.6. Satellite validation of CDOM algorithms

SeaWiFS merged local area coverage (MLAC) and MODIS-Aqua local area coverage (LAC) Level 1 files of the Northeast Atlantic are obtained from the NASA Ocean Color Web (<http://oceancolor.gsfc.nasa.gov/>). All files are processed to Level 2 using the standard defaults of SeaDAS 6.4, and masks are applied to pixels with any of the followings flags: land, cloud or ice, stray light, sun glint, high top-of-atmosphere radiance, low normalized water-leaving radiance at 555 or 547 nm, or atmospheric correction failure, according to Bailey and Werdell (2006). Satellite validation data collected within 3 h of the in situ sampling are extracted in  $3 \times 3$  native resolution pixel arrays centered on the field station locations (Fig. 1b). With the exception of the pixel array size extracted, all other satellite validation protocols are in accordance with those described in Bailey and Werdell (2006). For all the CDOM validation matchups, the average distance between the field station location and the center point of the center pixel in the  $3 \times 3$  validation pixel array is 0.66 km. The validation of algorithms is conducted with a completely independent dataset from the algorithm development dataset, i.e. data used in algorithm development are excluded from the validation analysis (Table 1; Fig. 1).

The evaluation of algorithm performance was based on statistical parameters comparing the satellite-derived retrievals of products with the field measurements, which are referred to here as validation matchups. The filtered means from the satellite  $3 \times 3$  pixel arrays were computed for comparison with field measurements:

$$\text{Filtered Mean} = [\sum_i (1.5 * \sigma - X) < x_i < (1.5 * \sigma + X)] / N \quad (7)$$

where X is the unfiltered mean value,  $\sigma$  is the standard deviation of the unfiltered values,  $x_i$  are the individual values for each  $3 \times 3$  pixel array, and N is the number of values from each  $3 \times 3$  pixel array that

falls within  $\pm 1.5 * \sigma$  (Bailey & Werdell, 2006). The coefficient of variation (CV) is computed from the filtered mean and standard deviation of values that pass the filtered criteria. Validation sites that exceed the mean filtered CV by  $>0.15$  are excluded from the validation analysis. A minimum of 5 pixels from the  $3 \times 3$  pixel arrays is required for inclusion of the matchup in the validation analysis.

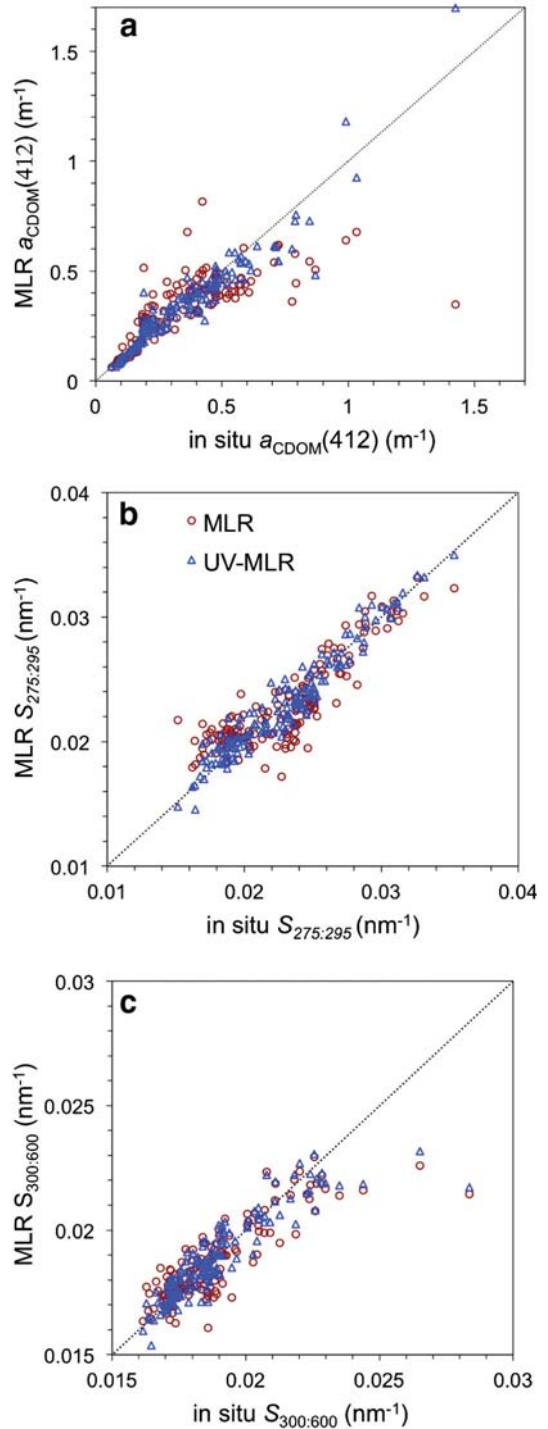


**Fig. 4.** Comparison of field measurements of (a)  $a_{CDOM}(412)$ , (b)  $S_{275:295}$  and (c)  $S_{300:600}$  with predicted values from multiple linear regression (MLR) algorithm of  $R_{rs}(443)$  and  $R_{rs}(547)$  for the red circles labeled MLR or with ultraviolet and other bands (MLR-UV) shown as blue triangles, which include  $R_{rs}(380)$ ,  $R_{rs}(412)$ ,  $R_{rs}(443)$ ,  $R_{rs}(490)$ ,  $R_{rs}(532)$ ,  $R_{rs}(547)$  and  $R_{rs}(665)$  for plots (a) and (c) and  $R_{rs}(380)$ ,  $R_{rs}(412)$ ,  $R_{rs}(443)$ ,  $R_{rs}(490)$  and  $R_{rs}(547)$  for plot (b). (For interpretation of the references to color in this figure legend, the reader is referred to the web version of this article.)

**Table 5**

Coefficients and goodness of fit parameter values from multiple linear regression-based (MLR) bio-optical  $a_{CDOM}$  algorithms developed from field observations of  $a_{CDOM}(\lambda)$  and remote sensing reflectance ( $R_{rs}(\lambda)$ ).  $Y = B_0 + B_1X_1 + B_2X_2 + B_3X_3 + B_4X_4 + B_5X_5 + B_6X_6 + B_7X_7$ ;  $X_{1...7} = \text{Ln}[R_{rs}(\lambda_{1...7})]$ ;  $Y = \text{Ln}[a_{CDOM}(\lambda)]$  or  $\text{Ln}[S_{CDOM}(\lambda_1;\lambda_2)]$ . Adj.  $R^2$  is the adjusted  $R^2$ , and MSE is the mean square error of the multiple linear regression analysis.

Multiple linear regression	$a_{CDOM275}$	$a_{CDOM355}$	$a_{CDOM380}$	$a_{CDOM412}$	$a_{CDOM443}$	$S_{275:295}$	$S_{300:600}$
<b>MODIS bands</b>							
$B_0 = \text{constant}$	0.464	-1.960	-2.507	-3.070	-3.664	-3.258	-3.640
$B_1: R_{rs443}$	-0.769	-1.208	-1.261	-1.285	-1.291	0.336	0.186
$B_2: R_{rs547}$	0.692	1.049	1.088	1.107	1.105	-0.279	-0.146
Adj. $R^2$	0.680	0.764	0.778	0.790	0.775	0.692	0.748
MSE	0.057	0.090	0.090	0.084	0.092	0.0096	0.0021
n	155	155	155	154	154	155	155
<b>SeaWiFS bands</b>							
$B_0 = \text{constant}$	0.643	-1.692	-2.227	-2.784	-3.379	-3.325	-3.679
$B_1: R_{rs443}$	-0.682	-1.076	-1.124	-1.146	-1.1513	0.300	0.168
$B_2: R_{rs555}$	0.630	0.954	0.990	1.008	1.006	-0.252	-0.134
Adj. $R^2$	0.670	0.751	0.765	0.777	0.762	0.674	0.740
MSE	0.059	0.095	0.095	0.089	0.097	0.010	0.0022
n	155	155	155	154	154	155	155
<b>UV and MODIS bands</b>							
$B_0 = \text{constant}$	0.4467	-2.092	-2.677	-3.176	-3.819	-3.085	-3.601
$B_1: R_{rs380}$	-0.5358	-0.604	-0.598	-0.530	-0.557	0.0747	
$B_2: R_{rs412}$	-0.4819	-1.265	-1.319	-1.423	-1.510	0.824	0.321
$B_3: R_{rs443}$	1.4978	2.575	2.667	2.714	3.000	-1.416	-0.449
$B_4: R_{rs490}$	-1.771	-2.479	-2.502	-2.513	-2.776	1.075	0.335
$B_5: R_{rs532}$	1.475	1.309	0.803	0.681	0.715		0.222
$B_6: R_{rs547}$	-0.4864		0.491	0.602	0.659	-0.459	-0.375
$B_7: R_{rs665}$	0.1726	0.215	0.190	0.200	0.185		
Adj. $R^2$	0.834	0.916	0.926	0.931	0.924	0.910	0.847
MSE	0.030	0.032	0.030	0.027	0.031	0.0028	0.0013
n	155	155	155	154	154	155	155

The statistical parameters applied for algorithm validation include the mean and standard deviation of the absolute percent difference (APD), root mean square error (RMSE), median ratio of computed filtered mean satellite value ( $C_{alg}$ ) to field measurement ( $C_{in situ}$ ), the semi-interquartile range (SIQR) and the  $R^2$  and slope values from linear regression analyses of the validation matchups for each satellite sensor (Bailey & Werdell, 2006).

$$\text{Mean APD}(\%) = \left[ \sum \left| \frac{C_{alg} - C_{in situ}}{C_{in situ}} \right| \right] * 100 / N \quad (8)$$

$$\text{RMSE} = \left[ 1/N * \sum (C_{alg} - C_{in situ})^2 \right]^{1/2} \quad (9)$$

**Table 6**

Coefficients and goodness of fit values for bio-optical  $a_{CDOM}$  algorithms developed from field observations of  $a_{CDOM}(\lambda)$  and light attenuation coefficients ( $K_d(\lambda)$ ).

Equation	$a_{CDOM355}$	$a_{CDOM380}$	$a_{CDOM412}$	$a_{CDOM443}$
$Y = A * X^B$	$A = 0.5097$	0.3307	0.1979	0.1145
$X = K_d(340)$	$B = 0.9321$	0.9431	0.936	0.9449
$Y = a_{CDOM}(\lambda)$				
$R^2$	0.952	0.953	0.955	0.947
Sy.x	0.1153	0.07594	0.0437	0.0283
n	148	148	148	149
$Y = A * X^B$	$A = 0.8325$	0.5409	0.3207	0.187
$X = K_d(380)$	$B = 0.7928$	0.8001	0.7961	0.8017
$Y = a_{CDOM}(\lambda)$				
$R^2$	0.884	0.8911	0.905	0.892
Sy.x	0.1818	0.1157	0.0635	0.0402
n	152	151	150	151
$Y = A * X^B$	$A = 1.021$	0.6680	0.4006	0.2311
$X = K_d(412)$	$B = 0.7076$	0.7165	0.7141	0.72
$Y = a_{CDOM}(\lambda)$				
$R^2$	0.818	0.8217	0.8472	0.8244
Sy.x	0.2151	0.1416	0.0770	0.0490
n	150	150	149	150

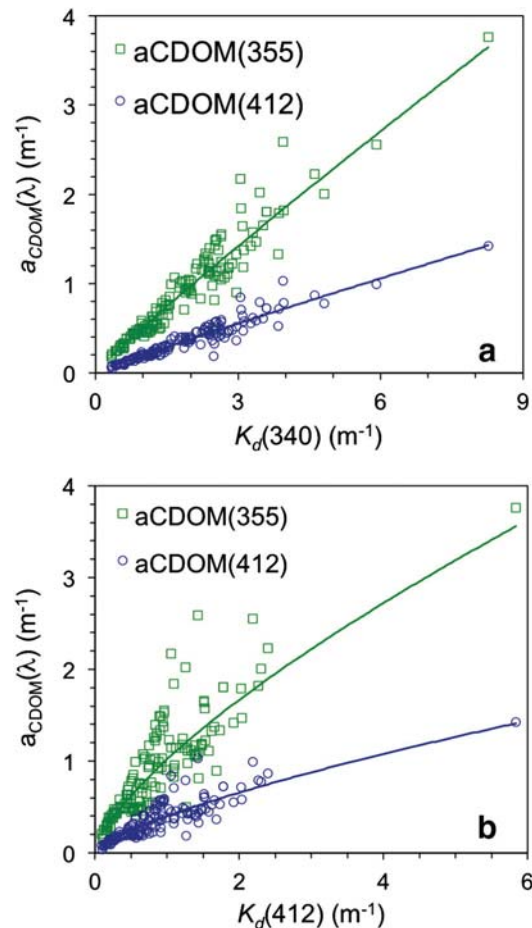


**Fig. 5.** Relationships of light attenuation coefficient at 340 nm (a)  $K_d(340)$  and at 412 nm (b)  $K_d(412)$  with  $a_{CDOM}(355)$  and  $a_{CDOM}(412)$  from field observations.

$$\% \text{ Bias} = \left[ \left( \frac{1}{N} * \sum (C_{\text{alg}} - C_{\text{in situ}}) \right) / \text{Mean} (C_{\text{in situ}}) \right] * 100 \quad (10)$$

$$\text{SIQR} = (Q_3 - Q_1) / 2 \quad (11)$$

where  $Q_3$  and  $Q_1$  represent the 75th and 25th percentiles for the ratios of the satellite-derived values to the field measurement.

### 3. Results

#### 3.1. Field distributions of CDOM properties

The spatial and seasonal distributions of  $a_{\text{CDOM}}$ ,  $S_{275:295}$  and  $S_{300:600}$  surface measurements collected from our cruises throughout the NES LME are presented in Table 2 (see Fig. 1c for a map of the sub-regions). These results show expected trends of decreasing  $a_{\text{CDOM}}$  and increasing  $S_{275:295}$  and  $S_{300:600}$  between the shore and continental slope for the Gulf of Maine and both MAB regions. The shallower areas of Georges Bank, a strong tidally mixed region, have higher  $a_{\text{CDOM}}$  and lower  $S_{275:295}$  and  $S_{300:600}$  than the deeper portions of Georges Bank. In the northern MAB (NMAB),  $a_{\text{CDOM}}$  on the inner- and mid-shelf peaked in spring while  $S_{275:295}$  was lowest, which coincides with peak river discharge. However, in the southern MAB (SMAB),  $a_{\text{CDOM}}$  was higher on average on the inner shelf in the fall and on the mid-shelf during summer. Note the high standard deviations for these values reaching ~50%

indicating high spatial and temporal variability in  $a_{\text{CDOM}}$ . Because some seasons and sub-regions were either not sampled or represented by too few stations and collected over 7 years, it is not possible to draw too many conclusions from these results especially for the outer shelf and continental slope areas and Gulf of Maine (Table 2), hence the utility of satellite observations.

#### 3.2. Algorithm development

##### 3.2.1. Band-ratio $a_{\text{CDOM}}(\lambda)$ algorithms

Multiple  $R_{rs}$  band-ratios yield strong relationships with  $a_{\text{CDOM}}(\lambda)$  for our northeastern U.S. coastal study region (Table 3). Prior work on  $a_{\text{CDOM}}$  algorithm development and validation for the southern MAB recommended a band-ratio algorithm of  $R_{rs}(490)/R_{rs}(555)$  and an exponential one-phase decay non-linear model (Mannino et al., 2008). However, as new field observations from the Gulf of Maine, Hudson estuary plume and New York Bight were added to the southern MAB dataset, it became clear that this band-ratio algorithm would not be appropriate across multiple regions (Fig. 2a). Applying the same non-linear model with a different band ratio,  $R_{rs}(412)/R_{rs}(555)$ , yielded a very good fit to the field observations for  $a_{\text{CDOM}}(412)$  (Fig. 2b;  $R^2 = 0.95$ ;  $Sy.x = 0.0806$ ) and other  $a_{\text{CDOM}}(\lambda)$  (Table A1). Other band ratios such as  $R_{rs}(412)/R_{rs}(547)$ ,  $R_{rs}(412)/R_{rs}(670)$ , and  $R_{rs}(412)/R_{rs}(665)$  (Fig. 2c) also yielded strong relationships for a broad range of  $a_{\text{CDOM}}(\lambda)$  (Table 2; Table A2). Although these algorithms have

**Table 7**

Satellite validation statistics of CDOM algorithms for SeaWiFS and MODIS-Aqua. Values and algorithms shown in bold represent algorithms with the best validation results. sd is the standard deviation of the MAPD. SIQR is the semi-interquartile range. MLR\_Fichot refers to an MLR algorithm published by Fichot et al. (2013).

Product	Algorithm	MAPD	± sd	RMSE	Median ratio	SIQR	%Bias	Slope	R <sup>2</sup>	n	
SeaWiFS	$a_{\text{CDOM}275}$	Exp_ $R_{rs}(412)/R_{rs}(670)$	26.2	24.9	1.76	0.94	<b>0.182</b>	−24.6	0.098	0.19	33
		QAA-based	43.4	26.1	2.03	0.91	0.417	−19.7	0.127	0.04	43
		MLR	27.3	<b>20.6</b>	<b>1.49</b>	<b>0.95</b>	0.225	− <b>18.4</b>	<b>0.395</b>	<b>0.53</b>	42
	$a_{\text{CDOM}355}$	Exp_ $R_{rs}(412)/R_{rs}(670)$	<b>28.1</b>	29.4	0.329	<b>0.96</b>	<b>0.189</b>	−25.9	0.133	0.21	33
		QAA-based	51.5	33.2	0.410	0.86	0.464	− <b>21.2</b>	0.168	0.06	43
		MLR	29.0	<b>21.9</b>	<b>0.305</b>	0.78	0.215	−29.0	<b>0.541</b>	<b>0.59</b>	42
	$a_{\text{CDOM}380}$	Exp_ $R_{rs}(412)/R_{rs}(670)$	<b>27.5</b>	27.4	0.200	<b>0.94</b>	0.218	−26.4	0.166	0.21	33
		QAA-based	51.4	32.7	0.262	0.80	0.450	− <b>20.8</b>	0.179	0.06	43
		MLR	29.1	<b>21.0</b>	<b>0.196</b>	0.75	<b>0.203</b>	−30.5	<b>0.567</b>	<b>0.61</b>	42
	$a_{\text{CDOM}412}$	Exp_ $R_{rs}(412)/R_{rs}(670)$	<b>27.7</b>	25.7	<b>0.114</b>	<b>0.90</b>	0.192	−27.1	0.179	0.22	33
		QAA-based	50.6	32.9	0.152	0.84	0.457	− <b>20.1</b>	0.188	0.064	43
		MLR	29.6	<b>19.0</b>	<b>0.113</b>	0.75	<b>0.182</b>	−31.0	<b>0.593</b>	<b>0.62</b>	42
	$a_{\text{CDOM}443}$	Exp_ $R_{rs}(412)/R_{rs}(670)$	<b>28.4</b>	25.6	0.0687	<b>0.86</b>	<b>0.163</b>	−29.5	0.165	0.23	33
		QAA-based	51.0	33.5	0.0877	<b>0.86</b>	0.472	− <b>20.1</b>	0.192	0.07	43
		MLR	30.0	<b>19.0</b>	<b>0.0650</b>	0.76	0.192	−31.0	<b>0.58</b>	<b>0.62</b>	42
	$S_{275:295}$	QAA-based	18.9	36.1	0.0079	<b>1.03</b>	0.097	9.1	−0.174	0.01	43
		MLR	<b>9.9</b>	<b>10.4</b>	<b>0.00318</b>	1.06	<b>0.042</b>	<b>7.5</b>	<b>0.545</b>	<b>0.44</b>	42
	$S_{300:600}$	QAA-based	<b>8.3</b>	9.1	0.00240	<b>1.03</b>	0.053	<b>6.0</b>	<b>0.642</b>	0.19	43
MLR		9.1	<b>6.0</b>	<b>0.00211</b>	1.07	<b>0.045</b>	7.2	0.264	0.10	42	
MODIS	$a_{\text{CDOM}275}$	Exp_ $R_{rs}(412)/R_{rs}(547)$	<b>23.4</b>	<b>17.1</b>	<b>0.952</b>	1.09	0.182	− <b>1.9</b>	0.270	0.37	53
		QAA-based	53.1	41.3	1.504	1.37	0.393	25.6	0.738	0.47	55
		MLR	24.3	18.1	1.086	<b>1.01</b>	0.214	−8.2	<b>0.532</b>	<b>0.58</b>	61
	$a_{\text{CDOM}355}$	Exp_ $R_{rs}(412)/R_{rs}(547)$	27.1	20.6	<b>0.186</b>	<b>1.01</b>	0.251	− <b>4.0</b>	0.360	0.39	53
		QAA-based	69.0	56.4	0.374	1.48	0.469	36.5	1.05	0.52	55
		MLR	<b>23.9</b>	<b>19.1</b>	0.212	0.87	<b>0.150</b>	−17.4	<b>0.626</b>	<b>0.76</b>	61
	$a_{\text{CDOM}380}$	Exp_ $R_{rs}(412)/R_{rs}(547)$	25.9	19.5	<b>0.118</b>	<b>0.99</b>	0.225	−5.4	0.379	0.40	53
		QAA-based	69.2	56.3	0.250	1.52	0.466	37.9	1.10	0.52	55
		MLR	<b>23.6</b>	<b>18.4</b>	0.134	0.85	<b>0.163</b>	−18.5	<b>0.658</b>	<b>0.76</b>	61
	$a_{\text{CDOM}412}$	Exp_ $R_{rs}(412)/R_{rs}(547)$	25.1	18.7	<b>0.0674</b>	<b>0.95</b>	0.194	−7.5	0.415	0.42	53
		QAA-based	66.7	55.6	0.149	1.53	0.438	37.7	1.13	0.51	55
		MLR	<b>22.7</b>	<b>17.0</b>	0.0760	0.85	<b>0.147</b>	−19.1	<b>0.702</b>	<b>0.77</b>	61
	$a_{\text{CDOM}443}$	Exp_ $R_{rs}(412)/R_{rs}(547)$	24.7	18.1	<b>0.0382</b>	<b>0.95</b>	0.186	−7.5	0.434	0.43	53
		QAA-based	67.4	54.8	0.0881	1.52	0.423	39.3	1.17	0.52	55
		MLR	<b>20.4</b>	<b>14.5</b>	0.0430	0.86	<b>0.138</b>	−18.6	<b>0.706</b>	<b>0.77</b>	49
	$S_{275:295}$	QAA-based	11.4	10.3	0.00390	0.92	0.072	−4.6	0.723	0.19	55
		MLR	8.7	6.4	0.00264	1.06	<b>0.044</b>	6.7	<b>1.02</b>	<b>0.64</b>	59
	$S_{300:600}$	MLR_Fichot	<b>7.2</b>	<b>5.8</b>	<b>0.00225</b>	<b>1.02</b>	0.054	<b>2.0</b>	1.05	0.54	52
QAA-based		<b>6.3</b>	7.2	<b>0.00180</b>	<b>1.01</b>	0.035	<b>1.4</b>	0.261	0.04	55	
	MLR	9.7	<b>4.2</b>	0.00197	1.10	0.036	8.2	<b>0.649</b>	<b>0.32</b>	59	

very high sensitivity for the lower  $a_{CDOM}$  values measured within our study region, they have little sensitivity at higher  $a_{CDOM}$  values typical of nearshore waters including the western Gulf of Maine, Hudson River Estuary, Chesapeake Bay and Delaware Bay. For instance, there is only a small change in the  $R_{rs}(412)/R_{rs}(555)$  value for  $a_{CDOM}(412)$  values between  $\sim 0.3$  and  $1 \text{ m}^{-1}$  of the non-linear model. A cubic polynomial fit of the natural log of  $a_{CDOM}(\lambda)$  with  $R_{rs}(412)/R_{rs}(555)$  yields similar results as the exponential one-phase decay model (results not shown). Band ratio algorithms where the blue band is replaced with an ultraviolet band (e.g., 340, 380 or 395 nm) yield similarly good relationships (data not shown), but also poor sensitivity at high  $a_{CDOM}$  values as the blue/green and blue/red band ratios.

### 3.2.2. IOP-based CDOM algorithms

The most promising set of algorithms relate  $a_{CDOM}(\lambda)$  to absorption products derived from QAA v5 (Lee et al., 2002, 2010). There is a strong positive relationship between  $a_{CDOM}(412)$  and the total absorption coefficient at 412 nm [ $a_t(412)$ ] derived using QAA from in situ  $R_{rs}$ , but a great deal of scatter at higher  $a_{CDOM}(412)$  values (Table 4;  $R^2 = 0.84$ ;  $Sy.x = 0.0754$ ). In contrast, the non-linear model fit of [ $a_t(412) - a_t(443)$ ] versus  $a_{CDOM}(\lambda)$  yielded a strong relationship across nearly three orders of magnitude of  $a_{CDOM}$  (Table 4; Fig. 3a). Although results for only five  $a_{CDOM}$  wavelengths are shown, the approach is applicable across a broad range of wavelengths such as from 250 to 450 nm. This approach also yields strong relationships between [ $a_t(412) - a_t(443)$ ] and CDOM spectral slopes,  $S_{275:295}$  and  $S_{300:600}$  (Fig. 3b; Table 4;  $R^2 = 0.75$ ;  $Sy.x = 0.00088$  and  $R^2 = 0.88$ ;  $Sy.x = 0.0014$ , respectively). The  $S_{275:295}$  relationship shows substantial scatter at high  $S_{275:295}$  values and thus may not be appropriate for [ $a_t(412) - a_t(443)$ ] greater than  $0.1 \text{ m}^{-1}$ . The  $S_{300:600}$  relationship loses sensitivity below  $0.02 \text{ nm}^{-1}$ . These algorithms are referred to as QAA-based algorithms throughout the remainder of this document.

### 3.2.3. Multiple linear regression CDOM algorithms

Bio-optical algorithms for several CDOM products were developed by applying multiple linear regression (MLR) analysis from field measurements of multiple  $R_{rs}$  bands to retrieve  $a_{CDOM}(\lambda)$ ,  $S_{275:295}$  and  $S_{300:600}$ . Initially, a stepwise backward statistical approach was applied using field-derived  $R_{rs}$  bands close to the band centers found on the SeaWiFS and MODIS-Aqua satellite sensors (443, 490, 510 or 531, 547 or 555, and 665 or 670 nm). The 412 nm band was not applied due to concerns of the high uncertainties in satellite retrievals of this particular band (e.g., Goyens, Jamet, & Schroeder, 2013). The MLR equation takes the following form:

$$Y = B_0 + B_1X_1 + B_2X_2 + B_3X_3 + \dots B_nX_n \quad (12)$$

where  $X_{1...n} = \text{Ln}[R_{rs}(\lambda_{1...n})]$ ,  $B_0 = \text{constant}$ ,  $B_1...B_n$  as coefficients for the  $R_{rs}$  bands, and  $Y = \text{Ln}[a_{CDOM}(\lambda)]$  or  $\text{Ln}(S)$ . The validation statistics of the satellite-retrieved values and independent field data for the stepwise backward algorithms requiring three to five  $R_{rs}$  bands were not as good as the guided MLR analysis using two  $R_{rs}$  bands (443 and 547 or 555 nm) (results not shown for the stepwise backward algorithms). The two-band MLR algorithm curve fitting results are encouraging (adjusted  $R^2 = 0.79$  and  $\text{MSE} = 0.084$  for  $a_{CDOM}(412)$ ; adjusted  $R^2 = 0.75$  and  $\text{MSE} = 0.0022$  for  $S_{300:600}$ ; Fig. 4; Table 5), though not as strong as the regression results from the band-ratio and QAA-based algorithms.

### 3.2.4. CDOM algorithms that employ ultraviolet radiometry

Ultraviolet radiometric measurements were incorporated into CDOM bio-optical algorithms to determine whether UV information would improve the accuracy of CDOM algorithms. Thus, the stepwise backward MLR analysis was applied to include several more bands in the blue and UV spectral range including 380, 395 and 412 nm plus the 5 other bands (443, 490, 532, 547 and 665 nm) discussed previously (UV-MLR). The goodness of fit statistics for these UV-MLR analyses

show a significant improvement from the MLR analyses that did not include the UV and 412 nm band (e.g., adjusted  $R^2 = 0.93$  and  $\text{MSE} = 0.027$  for  $a_{CDOM}(412)$ ; adjusted  $R^2 = 0.91$  and  $\text{MSE} = 0.0028$  for  $S_{275:295}$ ; adjusted  $R^2 = 0.85$  and  $\text{MSE} = 0.0013$  for  $S_{300:600}$ ; Fig. 4; Table 5). Plots of the field measurements versus the UV-MLR retrieved values demonstrate improvements in  $a_{CDOM}(412)$  retrievals (and for  $S_{275:295}$  and  $S_{300:600}$ ) across the full range of  $a_{CDOM}(412)$  measurements

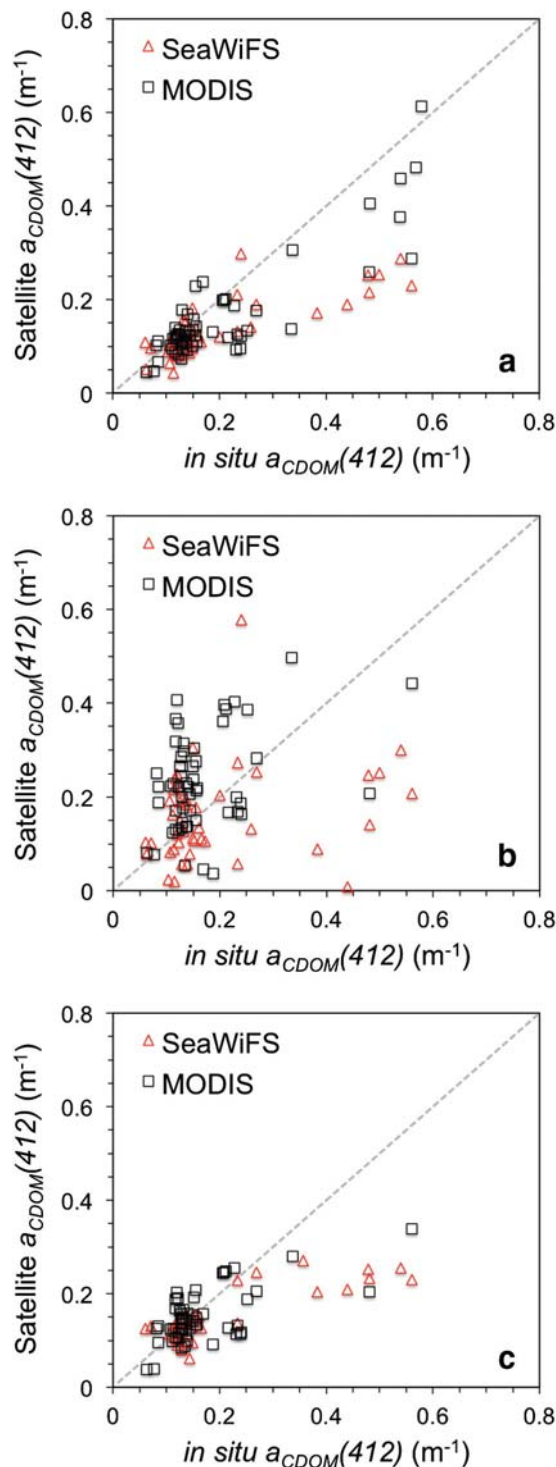


Fig. 6. Validation matchups of satellite-derived  $a_{CDOM}(412)$  products from SeaWiFS and MODIS-Aqua and field observations for (a) MLR, (b) QAA-based, and (c) exponential decay band ratios that applies the  $R_{rs}$  band ratios  $R_{rs}(412)/R_{rs}(547)$  for MODIS-Aqua and  $R_{rs}(412)/R_{rs}(670)$  for SeaWiFS (see Table 7 for validation statistics).

compared to the MLR retrievals, especially at the higher end of the range (Fig. 4). The MLR retrieved values shown in Fig. 4 were not obtained from an independent dataset from the data used to develop the MLR algorithms, but are included to demonstrate the potential of the MLR algorithms for both existing satellite sensors and planned future sensors. Since planned future sensors such as PACE and GEO-CAPE are not expected to provide  $R_{rs}$  below ~350 nm, the results for the UV-MLR with the 340 nm band are not shown here but are not significantly different than the results shown in Table 5.

Algorithms for  $a_{CDOM}(\lambda)$  were also developed through non-linear regression with the light attenuation coefficients,  $K_d(\lambda)$ , for blue (412 nm) and UV bands (340 and 380 nm), which were computed from in-water radiometry profiles. The relationships with  $K_d(340)$  yielded the strongest relationships with  $a_{CDOM}(\lambda)$  (for  $a_{CDOM}(412)$   $R^2 = 0.96$  and  $S_{y,x} = 0.044$ ), while the  $K_d(412)$  relationship was weakest ( $R^2 = 0.85$  and  $S_{y,x} = 0.077$ ; Table 6; Fig. 5).

### 3.3. Satellite validation of $a_{CDOM}(\lambda)$ and $S$ algorithms

Algorithm performance is evaluated with statistical parameters calculated from the filtered mean satellite data ( $R_{rs}$  and  $a_t$ ) and field measurements (Table 7). For both SeaWiFS and MODIS-Aqua, we validated multiple algorithms each for  $a_{CDOM}(275)$ ,  $a_{CDOM}(355)$ ,  $a_{CDOM}(380)$ ,  $a_{CDOM}(412)$ , and  $a_{CDOM}(443)$  and for other wavelengths (254, 295, 300, 360 nm) for which data is not shown because results were similar.  $K_d$  and UV-based MLR algorithms could not be validated due to the lack of necessary satellite products for  $a_{CDOM}(\lambda)$  retrieval ( $K_d$  or UV  $R_{rs}$  bands).

The validation statistics indicate that the QAA-based algorithm did not perform as well for satellite retrieval of  $a_{CDOM}(\lambda)$  as compared to the MLR and two band-ratio algorithms. The mean absolute percent difference (MAPD) and RMSE were consistently greater for the QAA-based algorithms for both SeaWiFS and MODIS-Aqua, ranging from  $43.4\% \pm 26.1$  and  $2.03 \text{ m}^{-1}$  for  $a_{CDOM}(275)$  to  $51.4\% \pm 32.7$  and  $0.26 \text{ m}^{-1}$  for  $a_{CDOM}(380)$  for SeaWiFS, and from  $53.1\% \pm 41.3$  and  $1.50 \text{ m}^{-1}$  for  $a_{CDOM}(275)$  to  $69.2\% \pm 56.3$  and  $0.25 \text{ m}^{-1}$  for  $a_{CDOM}(380)$  for MODIS (Table 7). For the QAA-based  $a_{CDOM}(\lambda)$  algorithms, both the MAPD and percent bias were greater for the MODIS validation than SeaWiFS.

Both the MLR and band-ratio algorithms performed well in retrieval of  $a_{CDOM}(\lambda)$ . Of the two band ratios, the  $\text{Exp-}R_{rs}(412)/R_{rs}(670)$  performed better for SeaWiFS retrieval of  $a_{CDOM}(\lambda)$ , and  $\text{Exp-}R_{rs}(412)/R_{rs}(547)$  performed better for MODIS (Table 7; Table A2). The preferable validation metrics of  $\text{Exp-}R_{rs}(412)/R_{rs}(670)$  for SeaWiFS are due to the exclusion of data values for which the SeaWiFS  $R_{rs}(670) 3 \times 3$  pixel array values did not meet the filtering criteria. The MLR algorithms performed better than the others when all the validation metrics are taken into account, particularly the slope and regression values from the linear regression of field measurements versus satellite-retrieved values (Fig. 6; Table 7). On average for all five  $a_{CDOM}(\lambda)$  MODIS retrievals, the MLR algorithm for MODIS yielded an MAPD of  $23.0\% \pm 17.4$ , median ratio of 0.89, SIQR of 0.162, bias of  $-16.4\%$ , slope of 0.64 and  $R^2$  of 0.73. For SeaWiFS, the average values for the validation metrics were MAPD of  $29.0\% \pm 20.3$ , median ratio of 0.80, SIQR of 0.203, bias of  $-28\%$ , slope of 0.54 and  $R^2$  of 0.59. The validation results for MODIS  $a_{CDOM}(\lambda)$  were generally better than for SeaWiFS, especially on bias, RMSE, slope and median ratio (Table 7; Fig. 6).

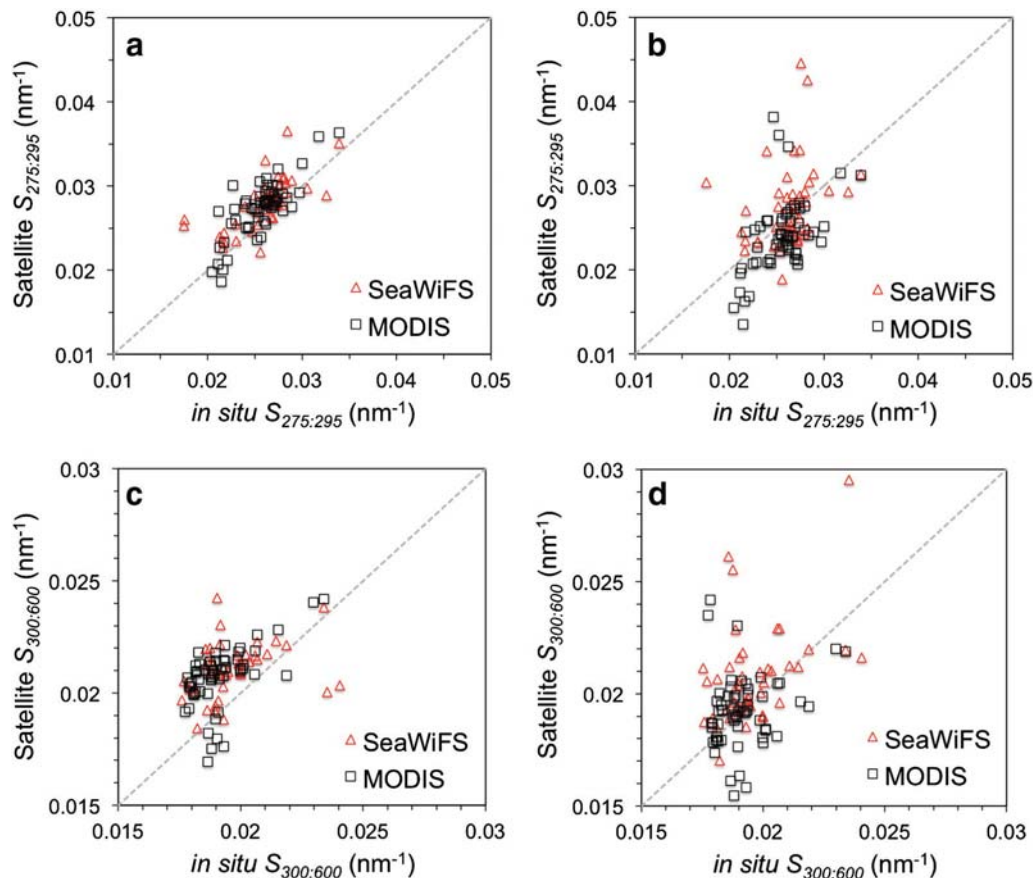


Fig. 7. Validation matchups of satellite-derived CDOM spectral slope products from SeaWiFS and MODIS-Aqua and field observations for (a) MLR  $S_{275:295}$ , (b) QAA-based  $S_{275:295}$ , (c) MLR  $S_{300:600}$ , and (d) QAA-based  $S_{300:600}$  products (see Table 7 for validation statistics).

**Table 8**  
Validation of SeaWiFS and MODIS-Aqua remote sensing reflectance ( $R_{rs}$ ) products.

Product	In situ band center (nm)	MAPD	$\pm$ sd	RMSE	Median ratio	SIQR	%Bias	Slope	R <sup>2</sup>	n
SeaWiFS										
$R_{rs}(412)$	412	101.9	86.7	0.00254	2.12	0.723	99.5	0.992	0.19	18
$R_{rs}(443)$	443	70.5	53.1	0.00203	1.72	0.520	68.0	1.02	0.24	19
$R_{rs}(490)$	490	36.5	21.2	0.00134	1.21	0.337	15.5	0.672	0.22	22
$R_{rs}(510)$	510	30.2	18.1	0.00110	1.08	0.279	8.42	0.618	0.34	25
$R_{rs}(555)$	555	29.7	23.1	0.00118	1.03	0.245	-1.65	0.583	0.39	28
$R_{rs}(670)$	670	60.9	71.3	0.000343	1.10	0.435	5.30	0.732	0.78	23
$R_{rs}(412)/R_{rs}(555)$		57.7	54.3	0.437	1.42	0.222	50.1	1.02	0.85	18
$R_{rs}(412)/R_{rs}(670)$		44.4	59.2	2.35	1.09	0.227	0.18	0.700	0.89	18
$R_{rs}(490)/R_{rs}(555)$		11.9	12.0	0.136	1.00	0.105	-1.25	0.838	0.94	22
MODIS-Aqua										
$R_{rs}(412)$	412	41.3	26.5	0.00113	0.77	0.233	-3.0	1.24	0.47	10
$R_{rs}(443)$	443	26.6	17.3	0.000935	0.85	0.202	-2.3	1.56	0.59	11
$R_{rs}(469)$	465	19.3	10.1	0.000799	0.82	0.150	-2.7	1.38	0.69	11
$R_{rs}(488)$	490	19.9	11.1	0.000930	0.77	0.133	-14.4	0.951	0.60	12
$R_{rs}(531)$	532	14.5	10.4	0.000865	0.86	0.087	-13.8	0.817	0.74	13
$R_{rs}(547)$	Modeled	15.3	10.7	0.000940	0.85	0.084	-15.8	0.764	0.74	13
$R_{rs}(555)$	555	23.2	12.8	0.00114	0.78	0.0963	-22.4	0.761	0.75	14
$R_{rs}(667)$	665	31.2	12.1	0.000224	0.67	0.0993	-21.0	1.07	0.81	13
$R_{rs}(667)$	670	38.9	11.2	0.000293	0.59	0.0779	-26.4	1.04	0.69	13
$R_{rs}(678)$	683	38.4	12.6	0.000318	0.65	0.116	-24.4	0.891	0.63	13
$R_{rs}(412)/R_{rs}(547)$	As above	36.6	22.0	0.316	0.92	0.293	9.8	1.30	0.92	9
$R_{rs}(412)/R_{rs}(667)$	665	42.9	63.3	5.667	0.96	0.266	54.8	1.55	0.93	9
$R_{rs}(488)/R_{rs}(547)$	As above	12.0	7.6	0.210	0.93	0.088	1.2	1.49	0.94	12

Validation statistics for the CDOM spectral slope algorithms were quite good for both sensors and algorithms evaluated. Excluding the QAA-based  $S_{275:295}$  algorithm, the validation statistics for the other  $S_{275:295}$  and  $S_{300:600}$  algorithms averaged  $8.5\% \pm 7$  for MAPD, 0.0023

for RMSE, 1.05 for the median ratio, 0.044 for SIQR, 5.6% for bias, 0.63 for slope and 0.32 for the R<sup>2</sup> (Table 7). For SeaWiFS, the QAA-based  $S_{300:600}$  algorithm performed slightly better statistically than the MLR algorithm, but the opposite was the case for MODIS (Fig. 7; Table 7).

**Table 9**

Spearman rank correlation values of SeaWiFS and MODIS-Aqua  $R_{rs}$  validation residuals versus various SeaWiFS and MODIS-Aqua parameters (atmospheric, sensor geometry, pixel size, etc.). P-value adjusted for number of comparisons,  $p = 0.05/13 = 0.00385$ .

SeaWiFS	solz	sens	NO <sub>2</sub> tropo	Epsilon	AOT 490	AOT 555	AOT 865	Angstrom	Time Diff	Pixel Size Y	Pixel Size X	Pixel Area	$R_{rs}(670)$
$R_{rs}(412)$	-0.721*	0.746*	ns	ns	0.785*	0.783*	0.747*	ns	ns	ns	0.708*	0.681*	ns
$R_{rs}(443)$	-0.711*	0.670*	ns	ns	0.806*	0.802*	0.767*	ns	ns	ns	0.638*	0.611^	ns
$R_{rs}(490)$	-0.645*	ns	-0.569^	ns	0.705*	0.701*	0.668*	ns	ns	ns	ns	ns	ns
$R_{rs}(510)$	-0.586*	ns	-0.560*	ns	0.679*	0.675*	0.625*	ns	ns	ns	ns	ns	ns
$R_{rs}(555)$	-0.651*	ns	-0.623*	ns	0.761*	0.757*	0.714*	ns	ns	ns	ns	ns	ns
$R_{rs}(670)$	-0.596*	ns	-0.645*	ns	0.692*	0.691*	0.642*	ns	ns	ns	ns	ns	ns
$R_{rs}(412)/R_{rs}(555)$	-0.646^	0.637^	ns	ns	0.730*	0.728*	0.726*	ns	ns	ns	0.608^	0.584^	ns
$R_{rs}(412)/R_{rs}(670)$	ns	ns	ns	ns	ns	ns	ns	ns	ns	ns	ns	ns	ns
$R_{rs}(490)/R_{rs}(555)$	ns	-0.425^	ns	ns	ns	ns	ns	ns	ns	ns	ns	-0.437^	0.537^
Mean	34.9	35.7	4.89E + 15	1.126	0.220	0.183	0.091	1.578	1.4	1.2	2.1	2.5	0.00099
sd	13.9	10.1	3.43E + 15	0.047	0.169	0.139	0.065	0.439	0.78	0.01	0.69	0.80	0.00060
n	28	28	28	28	28	28	28	27	28	28	28	28	23
MODIS-Aqua													
$R_{rs}(412)$	ns	ns	-0.783^	0.750^	ns	ns	ns	ns	ns	ns	ns	ns	ns
$R_{rs}(443)$	ns	ns	-0.645^	0.691^	ns	ns	ns	ns	0.673^	ns	ns	ns	ns
$R_{rs}(469)$	ns	ns	ns	ns	ns	ns	ns	ns	ns	ns	ns	ns	ns
$R_{rs}(488)$	ns	ns	ns	ns	ns	ns	ns	ns	ns	ns	ns	ns	ns
$R_{rs}(531)$	ns	ns	-0.626^	ns	ns	ns	ns	ns	ns	ns	ns	ns	ns
$R_{rs}(547)$	ns	ns	ns	ns	ns	ns	ns	ns	ns	ns	ns	ns	ns
$R_{rs}(555)$	ns	ns	-0.564^	ns	ns	ns	ns	ns	ns	ns	ns	ns	ns
$R_{rs}(667)$	ns	ns	-0.692^	ns	ns	ns	ns	ns	ns	ns	ns	ns	ns
$R_{rs}(667)$	ns	ns	-0.850*	ns	ns	ns	ns	ns	ns	ns	ns	ns	ns
$R_{rs}(678)$	-0.537^	ns	-0.749*	ns	ns	ns	ns	ns	ns	ns	ns	ns	ns
$R_{rs}(412)/R_{rs}(547)$	ns	ns	-0.883*	0.833^	ns	ns	ns	ns	ns	ns	ns	ns	ns
$R_{rs}(412)/R_{rs}(667)$	ns	ns	-0.717^	ns	ns	ns	ns	ns	ns	ns	ns	ns	ns
$R_{rs}(412)/R_{rs}(555)$	ns	ns	-0.883*	0.833^	ns	ns	ns	ns	ns	ns	ns	ns	ns
$R_{rs}(488)/R_{rs}(547)$	ns	ns	-0.776*	0.769*	ns	ns	ns	ns	ns	ns	ns	ns	ns
Mean	35.0	45.4	6.69 E + 15	1.15	0.16	0.141	0.079	1.33	1.18	1.42	2.70	4.01	7.47 E - 04
sd	12.7	9.5	3.18 E + 15	0.10	0.10	0.085	0.047	0.55	0.84	0.21	0.83	1.87	5.09 E - 04
n	15	15	15	15	15	15	15	15	15	15	15	15	13

solz = solar zenith angle, sens = sensor zenith angle; NO<sub>2</sub> tropo = tropospheric column NO<sub>2</sub> concentration; epsilon = ratio of aerosol reflectance for two NIR bands applied in aerosol model selection; AOT = aerosol optical thickness at wavelengths (nm) indicated; Angstrom = angstrom exponent of the aerosol model applied in L1 to L2 SeaDAS processing; Time Diff = time difference in hours between satellite observation and in situ sample collection; Pixel Size Y = pixel dimension from north to south in km; Pixel Size X = pixel dimension from east to west in km; Pixel Area = area of pixel in km<sup>2</sup>;  $R_{rs}(670)$  and  $R_{rs}(645)$  are applied here as a relative measure of suspended particle load; \* = significant at adjust p-value; ^ = significant at 0.05 level; ns = not significant.

We evaluated a second MLR algorithm for the MODIS  $S_{275:295}$  product (MLR\_Fichot), recently published by Fichot et al. (2013), that performed slightly better than our MLR algorithm (Table 7).

3.4. Satellite validation of  $R_{rs}$  products

In order to understand the potential causes of the poor validation performance of the QAA-based algorithms, we examined how well the satellite  $R_{rs}$  compared with the in situ  $R_{rs}$ . The validation metrics applied to the CDOM properties were also applied to the SeaWiFS and MODIS  $R_{rs}$  evaluation. The results reveal that the satellite  $R_{rs}$  products did not match the in situ  $R_{rs}$  well in most bands with MAPD ranging from  $29.7\% \pm 23.1$  for SeaWiFS  $R_{rs}(555)$  to  $102\% \pm 87$  for SeaWiFS  $R_{rs}(412)$  and from  $14.5\% \pm 10.4$  for MODIS  $R_{rs}(531)$  to  $41.3\% \pm 26.5$  for MODIS  $R_{rs}(412)$  (Table 8). The band ratios yielded similar results except for those based on  $R_{rs}(490)$  or  $R_{rs}(488)$ , which show relatively good agreement between satellite and field measurements. The other metrics generally show a similar pattern with the green satellite  $R_{rs}$  bands agreeing more closely to the in situ data than the blue and red bands (Table 8). One notable exception was in the MODIS average percent bias for  $R_{rs}(412)$ ,  $R_{rs}(443)$  and  $R_{rs}(469)$ , which were significantly less than for the other bands ( $-2.3$  to  $3\%$  compared to  $-13.8\%$  to  $-26.4\%$ ). Some of these results may be related to the relatively small sample size of 9 for MODIS-Aqua to 28 matchups for SeaWiFS. Nevertheless, Goyens et al. (2013) examined 364 coastal matchups of MODIS-Aqua and in situ data and obtained similar results with MAPD of 11–13% for water leaving radiances at 488, 531 and 547 nm and 21–35% at 412, 443 and 667 nm for the same atmospheric correction processing applied in this study.

3.5. Evaluation of factors that could influence satellite product uncertainty

To explore the possible factors that influence SeaWiFS and MODIS retrievals for our study region, Spearman rank correlation analyses were conducted on the residuals for satellite-in situ  $R_{rs}$  matchups ( $C_{sat} - C_{in\ situ}$ ) with the many parameters that could influence the uncertainty of satellite  $R_{rs}$  retrievals such as solar or sensor geometry, atmospheric aerosol and trace gas properties, spatial and temporal mismatch between satellite overpass and in situ measurements, and surface water turbidity (from  $R_{rs}(670)$  and  $R_{rs}(645)$ , for SeaWiFS and MODIS, respectively). A statistically significant positive correlation would suggest that the satellite  $R_{rs}$  is lower than the in situ measurements at low values of the correlative parameter and greater than in situ at higher values of the correlative parameter. For a negative correlation result, satellite  $R_{rs}$  are higher than the in situ measurements at low values of the correlative parameter and lower than in situ at higher values of the correlative parameter. A significant correlation between the residuals and a particular parameter does not constitute a causation of the errors in the matchups, but rather at topic to investigate further. A subset of these comparisons reveals that atmospheric properties as well as solar zenith angle (SZA), sensor zenith angle and pixel resolution are highly correlated with the residuals of  $R_{rs}$  from SeaWiFS (Table 9). Specifically, the residuals for the SeaWiFS matchups are significantly correlated to SZA (negative correlation) and to aerosol optical thickness (AOT; positive correlation) for all the  $R_{rs}$  bands, but only a subset of the bands for sensor zenith angle (positively except for  $R_{rs}(490)/R_{rs}(555)$ ), tropospheric column  $NO_2$  concentrations ( $NO_2$  tropo; negative correlation), and pixel size x (east to west dimension) and pixel area (positive correlation). For MODIS, only the tropospheric column  $NO_2$  concentrations ( $NO_2$  tropo) and epsilon are significantly correlated to the  $R_{rs}$  residuals, with the exception of SZA for  $R_{rs}(678)$  and time difference for  $R_{rs}(443)$  (Table 9). The small sample size likely limits the robustness of the MODIS  $R_{rs}$  correlation analysis.

The Spearman rank correlation analysis was also conducted on the residuals of the validation matchups from each of the CDOM and spectral slope algorithms. For the SeaWiFS  $a_{CDOM}(355)$  and  $a_{CDOM}(412)$

**Table 10** Spearman rank correlation values of SeaWiFS  $a_{CDOM}(412)$ ,  $a_{CDOM}(355)$ ,  $S_{275:295}$ , and  $S_{300:600}$  validation residuals versus various SeaWiFS parameters (atmospheric, sensor geometry, pixel size, etc.). P-value adjusted for number of comparisons,  $p = 0.05/15 = 0.00333$ . See Table 9 for further details.

Product	Algorithm	solz	senz	Ozone	$NO_2$ tropo	$NO_2$ strat	Epsilon	AOT 490	AOT 555	AOT 865	Angstrom	Time Diff	Pixel Size Y	Pixel Size X	Pixel Area	$R_{rs}$ (670)
$a_{CDOM}(412)$	QAA-based	0.337^	-0.310^	ns	-0.529*	ns	ns	-0.642*	-0.654*	-0.681*	0.518*	ns	ns	ns	ns	-0.531*
	Exp_ $R_{rs}(412)/R_{rs}(670)$	ns	-0.508*	ns	-0.665*	ns	0.494^	-0.504*	-0.517*	-0.643*	0.600*	ns	0.360^	-0.400^	-0.414^	-0.497*
	MLR	0.439^	ns	ns	-0.485*	ns	0.376^	-0.535*	-0.547*	-0.613*	0.565*	ns	ns	ns	-0.458^	ns
$a_{CDOM}(355)$	QAA-based	0.381^	-0.317^	ns	-0.499*	ns	ns	-0.681*	-0.691*	-0.710*	0.509*	ns	ns	ns	ns	-0.496*
	Exp_ $R_{rs}(412)/R_{rs}(670)$	ns	-0.399^	ns	-0.635*	ns	0.581*	-0.499*	-0.509*	-0.632*	0.578*	ns	ns	ns	ns	-0.532*
	MLR	0.481*	ns	ns	-0.398^	ns	0.354^	-0.597*	-0.604*	-0.642*	0.512*	ns	ns	ns	-0.409^	ns
$S_{300:600}$	QAA-based	ns	ns	ns	0.397^	-0.339^	ns	ns	ns	ns	-0.321^	ns	-0.362^	ns	ns	ns
	MLR	0.405^	ns	ns	ns	-0.367^	ns	-0.521*	-0.504*	-0.381^	ns	ns	-0.324^	ns	ns	ns
$S_{275:295}$	QAA-based	ns	0.320^	ns	0.518*	ns	ns	0.471*	0.488*	0.530*	-0.455*	ns	-0.303^	ns	ns	0.364^
	MLR	ns	ns	ns	0.398^	ns	ns	ns	ns	ns	ns	ns	ns	ns	ns	ns
Mean	MLR	42.3	36.8	0.315	3.24 E + 15	2.99 E + 15	1.15	0.144	0.120	0.059	1.622	1.43	1.15	2.28	2.62	0.00100
	MLR	16.1	12.2	0.035	1.14 E + 15	5.68 E + 14	0.04	0.078	0.065	0.035	0.367	0.88	0.01	0.92	1.03	0.00106
sd	MLR	42	42	42	42	42	42	42	42	42	40	42	42	42	42	36

Ozone = atmospheric total column ozone;  $NO_2$  strat = stratospheric column  $NO_2$  concentration.

**Table 11**  
Spearman rank correlation values of MODIS-Aqua  $a_{CDOM(412)}$ ,  $a_{CDOM(355)}$ ,  $S_{275:295}$ , and  $S_{300:600}$  validation residuals versus various MODIS parameters (atmospheric, sensor geometry, pixel size, etc.), P-value adjusted for number of comparisons,  $p = 0.05/15 = 0.00333$ . See Table 9 for further details.

Product	Algorithm	solz	senz	Ozone	NO <sub>2</sub> tropo	NO <sub>2</sub> strat	Epsilon	AOT 488	AOT 547	AOT 869	Angstrom	Time Diff	Pixel Size Y	Pixel Size X	Pixel Area	Rrs (645)
$a_{CDOM(412)}$	QAA-based	ns	-0.320 <sup>^</sup>	ns	ns	ns	-0.535*	ns	ns	ns	-0.400*	ns	-0.351 <sup>^</sup>	-0.342 <sup>^</sup>	-0.365 <sup>^</sup>	ns
	Exp_Rrs412/Rrs547	0.372 <sup>^</sup>	ns	ns	ns	ns	-0.595*	-0.504*	ns	ns	-0.573*	ns	ns	ns	ns	ns
	MLR	0.532*	ns	-0.379 <sup>^</sup>	ns	-0.539*	-0.307 <sup>^</sup>	-0.647*	-0.631*	-0.451*	-0.475*	ns	ns	ns	ns	ns
$a_{CDOM(355)}$	QAA-based	ns	-0.306	ns	ns	ns	-0.539*	ns	ns	ns	-0.433*	ns	-0.336 <sup>^</sup>	-0.328 <sup>^</sup>	ns	ns
	Exp_Rrs412/Rrs547	0.440*	ns	ns	ns	-0.311 <sup>^</sup>	-0.623*	-0.607*	-0.575*	-0.290 <sup>^</sup>	-0.663*	ns	ns	ns	ns	ns
	MLR	0.587*	ns	-0.431 <sup>^</sup>	ns	-0.609*	-0.358 <sup>^</sup>	-0.688*	-0.674*	-0.468*	-0.580*	ns	ns	ns	ns	ns
$S_{300:600}$	QAA-based	ns	0.278 <sup>^</sup>	-0.344 <sup>^</sup>	ns	-0.338 <sup>^</sup>	0.285 <sup>^</sup>	ns	-0.283 <sup>^</sup>	-0.310 <sup>^</sup>	ns	ns	0.332 <sup>^</sup>	0.314 <sup>^</sup>	0.350 <sup>^</sup>	ns
	MLR	ns	ns	ns	ns	ns	ns	ns	ns	ns	ns	ns	ns	ns	ns	-0.278 <sup>^</sup>
	QAA-based	ns	0.266 <sup>^</sup>	ns	ns	ns	0.539*	ns	ns	ns	0.293 <sup>^</sup>	ns	0.298 <sup>^</sup>	0.287 <sup>^</sup>	0.320 <sup>^</sup>	ns
$S_{275:295}$	MLR	-0.469*	ns	0.447*	ns	0.533*	0.321 <sup>^</sup>	0.489*	0.466*	ns	0.431*	ns	ns	ns	ns	-0.515*
	Fichot MLR	-0.499*	ns	0.568*	ns	0.573*	ns	0.445*	0.417*	ns	0.458*	ns	ns	ns	ns	-0.617*
	MLR	40.7	31.7	0.314	3.2 E + 15	2.9 E + 15	1.154	0.138	0.117	0.059	1.382	1.389	1.388	2.163	3.335	0.00147
Mean	MLR	16.5	18.6	0.035	1.4 E + 15	6.6 E + 14	0.081	0.078	0.064	0.029	0.546	0.894	0.628	0.868	2.887	0.00202
sd	MLR	61	61	61	61	61	61	61	61	61	60	61	61	61	61	57
n	MLR	61	61	61	61	61	61	61	61	61	61	61	61	61	61	57

algorithms, the residuals are negatively correlated with NO<sub>2</sub> tropo, AOT and R<sub>rs</sub>(670), but positively correlated with the angstrom exponent (Table 10). The results are similar for all of the  $a_{CDOM}$  algorithms evaluated. The correlations for the SeaWiFS spectral slope algorithms only show significant correlations for the MLR  $S_{300:600}$  with AOT and the QAA-based  $S_{275:295}$  algorithm with NO<sub>2</sub> tropo, AOT and angstrom.

The correlation analyses for the MODIS CDOM products yield somewhat different results. The residuals of the QAA-based  $a_{CDOM}(355)$  and  $a_{CDOM}(412)$  algorithms are negatively correlated with epsilon and angstrom whereas the band-ratio and MLR residuals are significantly correlated with SZA (positive correlation) and negatively correlated with stratospheric column NO<sub>2</sub> (NO<sub>2</sub> strat), AOT and angstrom (Table 11). The correlations with epsilon are also significant and negative for the band-ratio algorithm residuals. The QAA-based  $S_{275:295}$  residuals are only correlated with epsilon at the adjusted P-value threshold, and the MLR  $S_{275:295}$  residuals are correlated to SZA (negative), ozone (positive), NO<sub>2</sub> strat (positive), AOT (positive), angstrom (positive), and R<sub>rs</sub>(645) (negative). However, neither of the  $S_{300:600}$  algorithm residuals are significantly correlated (at the adjusted p-value) with any of the parameters investigated.

### 3.5. Extrapolation of CDOM properties in the UV

Information on CDOM in the UV can be extrapolated from visible band reflectances because of the strong correlation between  $a_{CDOM}(\lambda)$  with  $a_{CDOM}$  at other wavelengths such as  $a_{CDOM}(412)$  (Fig. 8). The Pearson correlation analysis between  $a_{CDOM}(412)$  and  $a_{CDOM}(250:600)$  of over 1900 discrete samples from our study region shows that the correlation coefficient (R) varies from a minimum of 0.76 at 599 nm, 0.89 at 250 nm and >0.950 between 296 nm and 511 nm (Fig. 8). If we limit our data geographically to only the southern MAB and by season (combined fall, winter, spring), then the R-value is significantly higher at the lower and higher wavelengths (0.99 at 250 nm and 0.97 at 530 nm).

### 3.6. Evaluation of satellite-derived CDOM properties

To further evaluate the applicability of the  $a_{CDOM}(\lambda)$ ,  $S_{300:600}$ , and  $S_{275:295}$  MLR algorithms, temporal and spatial trends of SeaWiFS- and MODIS-derived CDOM products were compared with field measurements. Several time series of daily MODIS-Aqua and SeaWiFS  $a_{CDOM}(412)$ ,  $S_{275:295}$ , and  $S_{300:600}$  were generated for four locations from the lower Chesapeake Bay, bay mouth, plume and adjacent shelf waters that were sampled multiple times from 2004 to 2007. Although the sampling dates are not coincident with the satellite observations

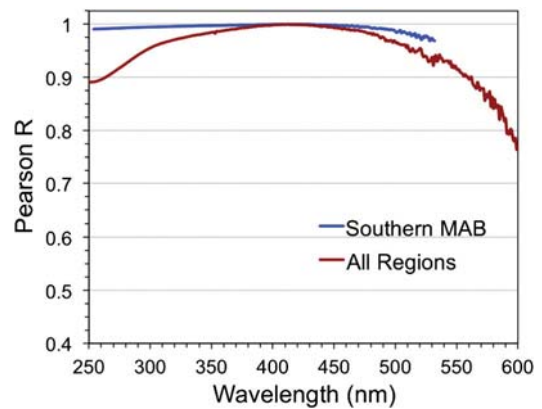


**Fig. 8.** Pearson correlation coefficient values (R) for the comparison of  $a_{CDOM}(412)$  versus  $a_{CDOM}(\lambda)$  from 250 to 600 nm. Data for all regions represent a compilation of 1933 discrete samples collected at various depths within estuaries and continental margin of the northeastern U.S. see Fig. 1c and Table 1 for geographic distributions and dates of sample collections.

(with a couple of exceptions), the results show that satellite-derived  $a_{CDOM(412)}$ ,  $S_{275:295}$ , and  $S_{300:600}$  (not shown) do capture the general trends and variability of CDOM properties (Fig. 9). Despite the fact that no data from the lower Chesapeake Bay site were included in the algorithm development due to the absence of radiometry data, our algorithms were able to capture the dynamic range for this site. In addition, multi-year mean monthly composites (2004–2007) of satellite  $a_{CDOM(412)}$  and  $S$  were computed for each of the sub-regions (Fig. 1c) for comparison with field measurement averaged across each sub-region. The monthly composite plots demonstrate that the spatial and temporal trends in the satellite data are equivalent to those from the field data to within the uncertainty of the validation statistics (Fig. 10;

only MODIS-Aqua results shown). Note that the sample size for the mean monthly field measurements is quite low (Table 2; Fig. 10).

SeaWiFS and MODIS-Aqua monthly composites of  $a_{CDOM(412)}$ ,  $S_{275:295}$  and  $S_{300:600}$  were processed for multiple years (2004–2007) with the better performing MLR and band-ratio algorithms for  $a_{CDOM(412)}$  and MLR and QAA-based algorithms for  $S_{275:295}$  and  $S_{300:600}$  to examine the performance of algorithms with respect to the spatial and temporal variability of these CDOM properties. The processed monthly satellite images (only 2006 presented) demonstrate that these algorithms can be applied to generate SeaWiFS and MODIS-Aqua maps of these CDOM properties (Figs. 11–13). The satellite distributions of  $a_{CDOM(412)}$  appear quite reasonable based on our field measurements and the processes

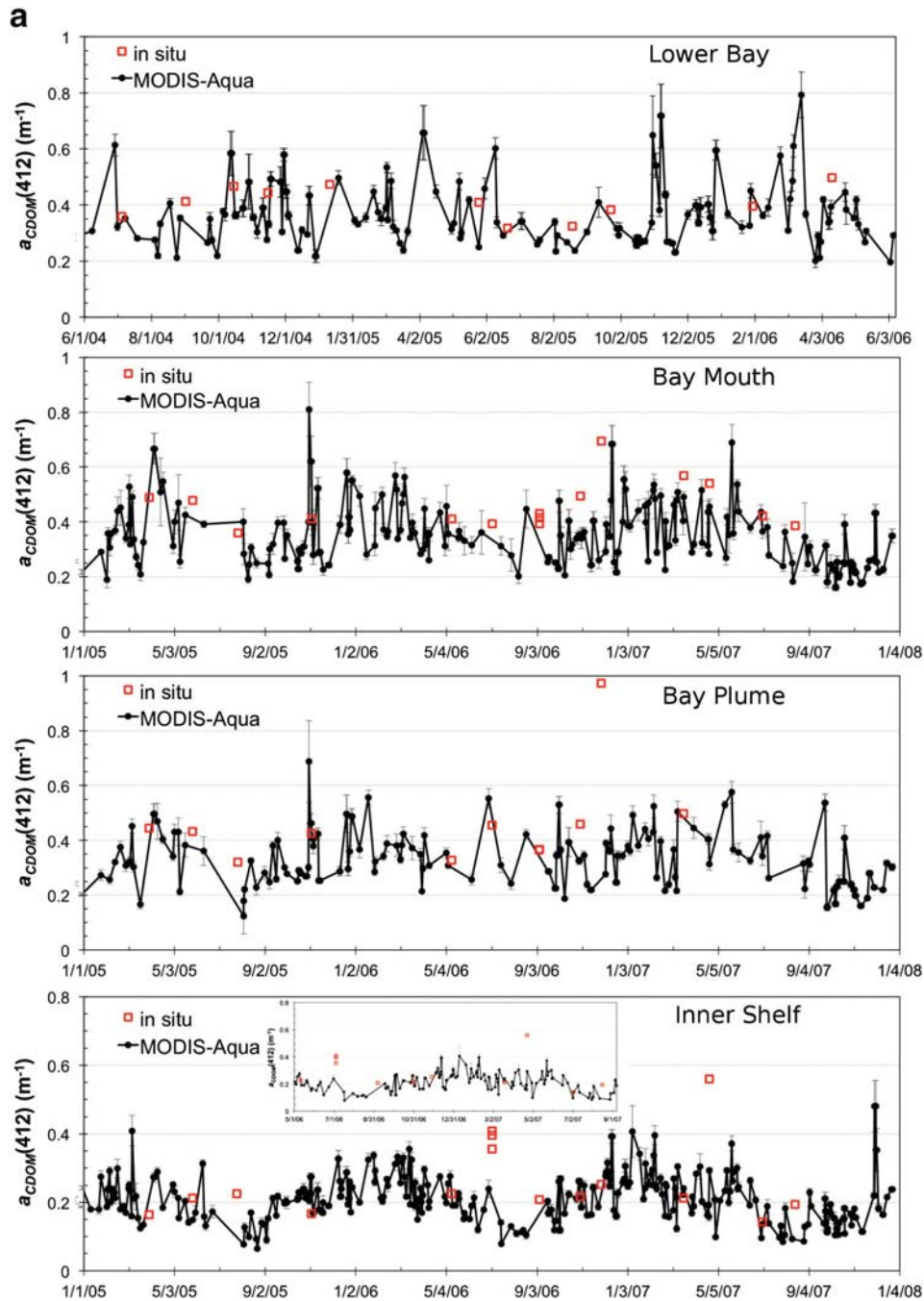


**Fig. 9.** Multi-year time series comparisons of field measurements and (a) daily MODIS-Aqua  $a_{CDOM(412)}$ , (b) SeaWiFS  $a_{CDOM(412)}$ , and (c) MODIS-Aqua  $S_{275:295}$  for sites located in the lower Chesapeake Bay, mouth of the bay, plume, and inner shelf (see Fig. 1c). The error bars on the satellite data represent the standard deviation of the  $3 \times 3$  satellite pixel array centered on the field station location. Note that field measurements do not coincide with the day and time of the satellite data (with a few rare exceptions). On a few occasions, multiple samples were collected at a station over the course of 45 min to 1 h, which is why some plots show three field data points for the same date.

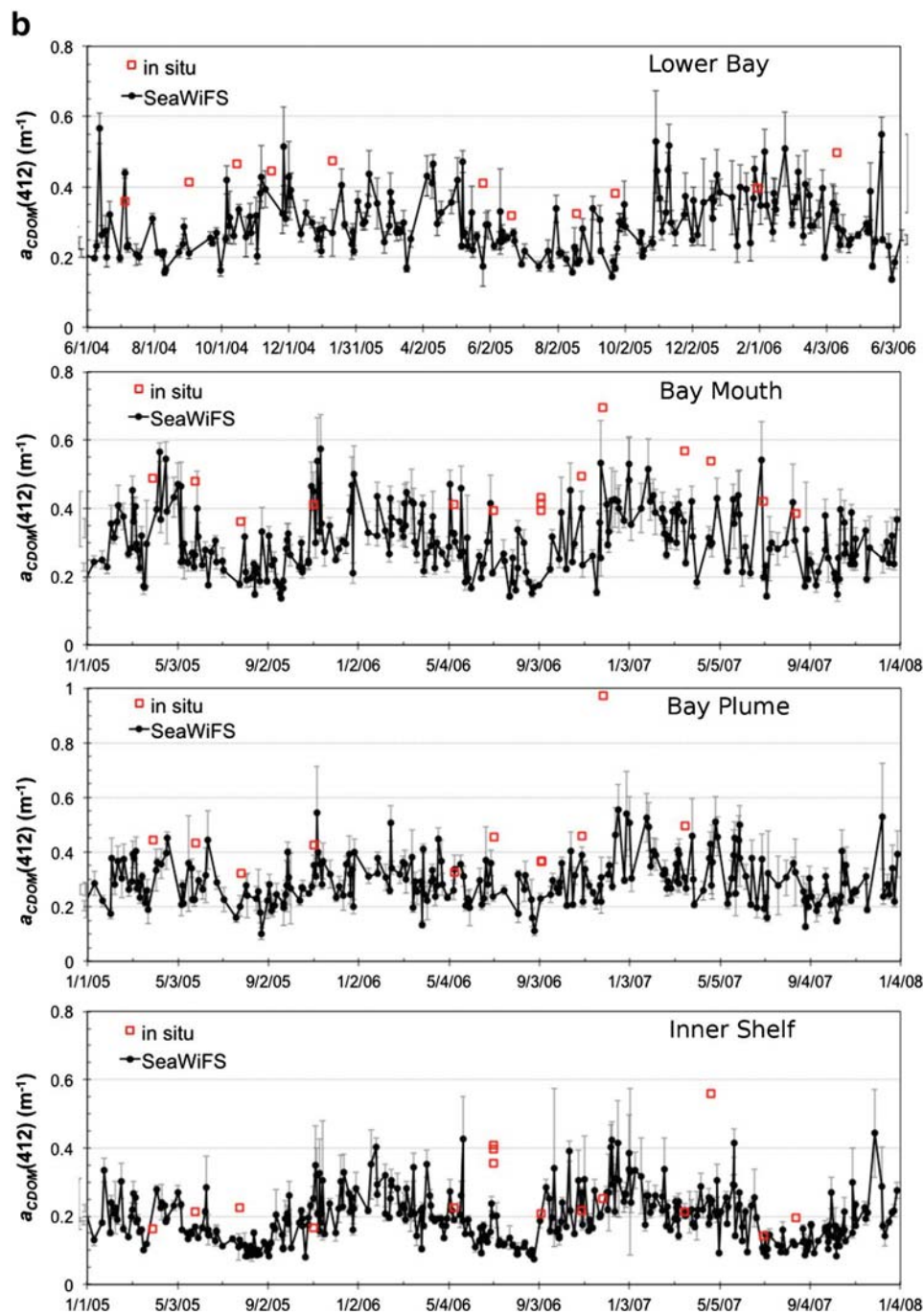


Fig. 9 (continued).

that impact CDOM levels along the continental shelf of the northeastern U.S. (Table 2; see Section 4.3). Both field measurements and satellite data show a decrease in  $a_{CDOM}(412)$  along a gradient from nearshore to offshore and from north-to-south between the Gulf of Maine and southern MAB, excluding Georges Bank (Figs. 10–11; Table 2).  $a_{CDOM}(412)$  is generally higher in spring and fall and lowest during summer. The satellite and field data for both  $S_{275:295}$  and  $S_{300:600}$  demonstrate similar spatial and temporal trends with both  $S_{275:295}$  and  $S_{300:600}$  decreasing from nearshore to offshore and from north-to-south (excluding Georges Bank) and generally higher values in summer than other seasons (Figs. 10b, 12–13; Table 2). For both  $S_{275:295}$  and  $S_{300:600}$ , the SeaWiFS and MODIS QAA-based values are much lower than the MLR values across all seasons (Figs. 12–13).

## 4. Discussion

### 4.1. Algorithm performance

Using in situ radiometry and CDOM absorption and spectral slope measurements, we developed and tuned several types of algorithms for  $a_{CDOM}(\lambda)$ ,  $S_{275:295}$  and  $S_{300:600}$  which included several band-ratio algorithms, QAA-based, MLR and  $K_d(\lambda)$  relationships. The in situ data show that these algorithms were applicable across the entire study region with the exception of the exponential decay band ratio of  $R_{rs}(490)/R_{rs}(555)$ , which required different tuning coefficients for the three sub-regions, western Gulf of Maine, New York Bight (region between northern New Jersey and Long Island), and southern MAB,

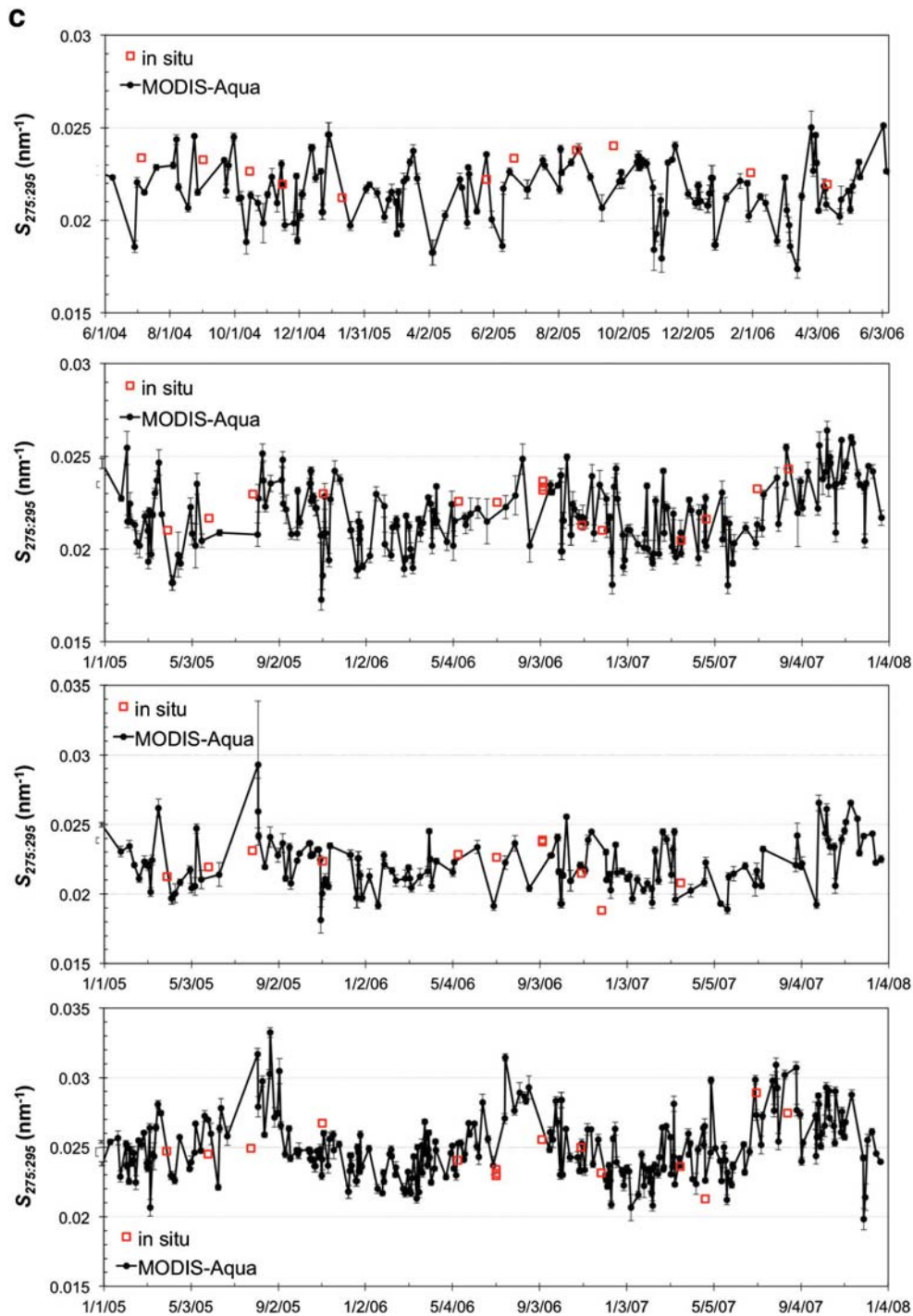


Fig. 9 (continued).

where we had both in situ radiometry and CDOM measurements (Figs. 1a and 2a). Since the band ratio algorithms containing the 412 nm band yielded good relationships across all regions, this would suggest that contribution of phytoplankton to  $R_{rs}(490)$  somehow differs among the three sub-regions yielding the three different band ratio relationships presented in Fig. 2a. The concentration and composition of phytoplankton carotenoid pigments (and potentially chlorophylls *b* and *c*) could impact  $R_{rs}(490)$  in areas where phytoplankton are present in appreciable abundances as are typical for the study region. Differences in phytoplankton species composition between these regions and potentially pigment packaging among the different species are the likely causes of the divergent relationships of  $R_{rs}(490)/R_{rs}(555)$

with  $a_{CDOM}(412)$  (Fig. 2a). Thus, the  $R_{rs}(490)/R_{rs}(555)$  band ratio is not recommended for retrieval of  $a_{CDOM}(\lambda)$ .

Our results demonstrate several robust in situ bio-optical algorithms to quantify  $a_{CDOM}(\lambda)$ ,  $S_{275:295}$  and  $S_{300:600}$  (Tables 3–6) as well as the validation of these algorithms for the SeaWiFS and MODIS-Aqua sensors (Table 7; Figs. 6–7). Despite the robustness of the bio-optical algorithms illustrated for the field measurements, the satellite retrievals of  $a_{CDOM}(\lambda)$  for some of the algorithms were not as good as one would expect based on our algorithm development results (Tables 3–7). In particular, the QAA-based algorithm is one algorithm that seemed to fit the field measurements quite well (Fig. 3a; Table 4), but performed poorly in the satellite retrievals of CDOM properties (Fig. 7; Table 7).

The validation results for the band ratio and MLR algorithms demonstrate that these algorithms are appropriate for SeaWiFS and MODIS retrieval of  $a_{CDOM}(\lambda)$  and the MLR algorithms for retrieval of  $S_{275:295}$  and  $S_{300:600}$  (Table 7). The QAA-based CDOM spectral slopes were insensitive to changes in  $[a_t(412) - a_t(443)]$  at lower  $S_{275:295}$  and  $S_{300:600}$  values. For SeaWiFS, the MLR and Exp\_ $R_{rs}(412)/R_{rs}(670)$  algorithms performed

better for  $a_{CDOM}(\lambda)$  than the other algorithms, and for MODIS, the MLR and Exp\_ $R_{rs}(412)/R_{rs}(547)$  performed better. Because the band ratio algorithms lose sensitivity at higher and lower  $a_{CDOM}(\lambda)$  concentrations (Fig. 2), the MLR algorithm is recommended because it can be applied to regions with high and low  $a_{CDOM}(\lambda)$  such as estuaries and ocean waters beyond the continental margin. The satellite distributions of

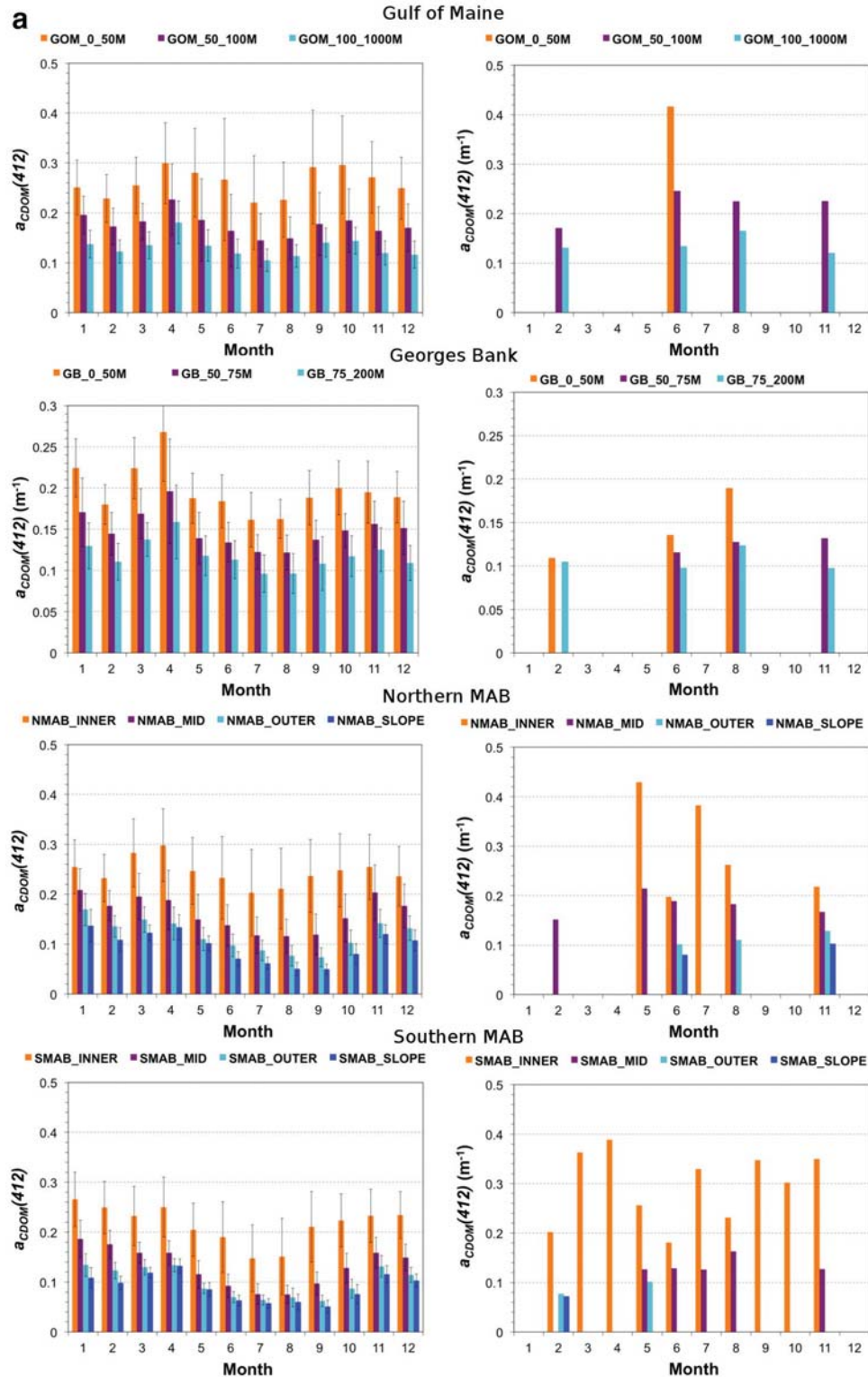


**Fig. 10.** Comparison of multi-year (2004–2007) averaged monthly MODIS-Aqua composites (left panels) and field observations (2004–2013; right panels) of (a)  $a_{CDOM}(412)$  and (b)  $S_{275:295}$  by sub-region. The error bars shown on the MODIS data plots represent the standard deviation of the satellite pixels within each sub-region. Sample size for averaged monthly field observations was  $\geq 5$ .

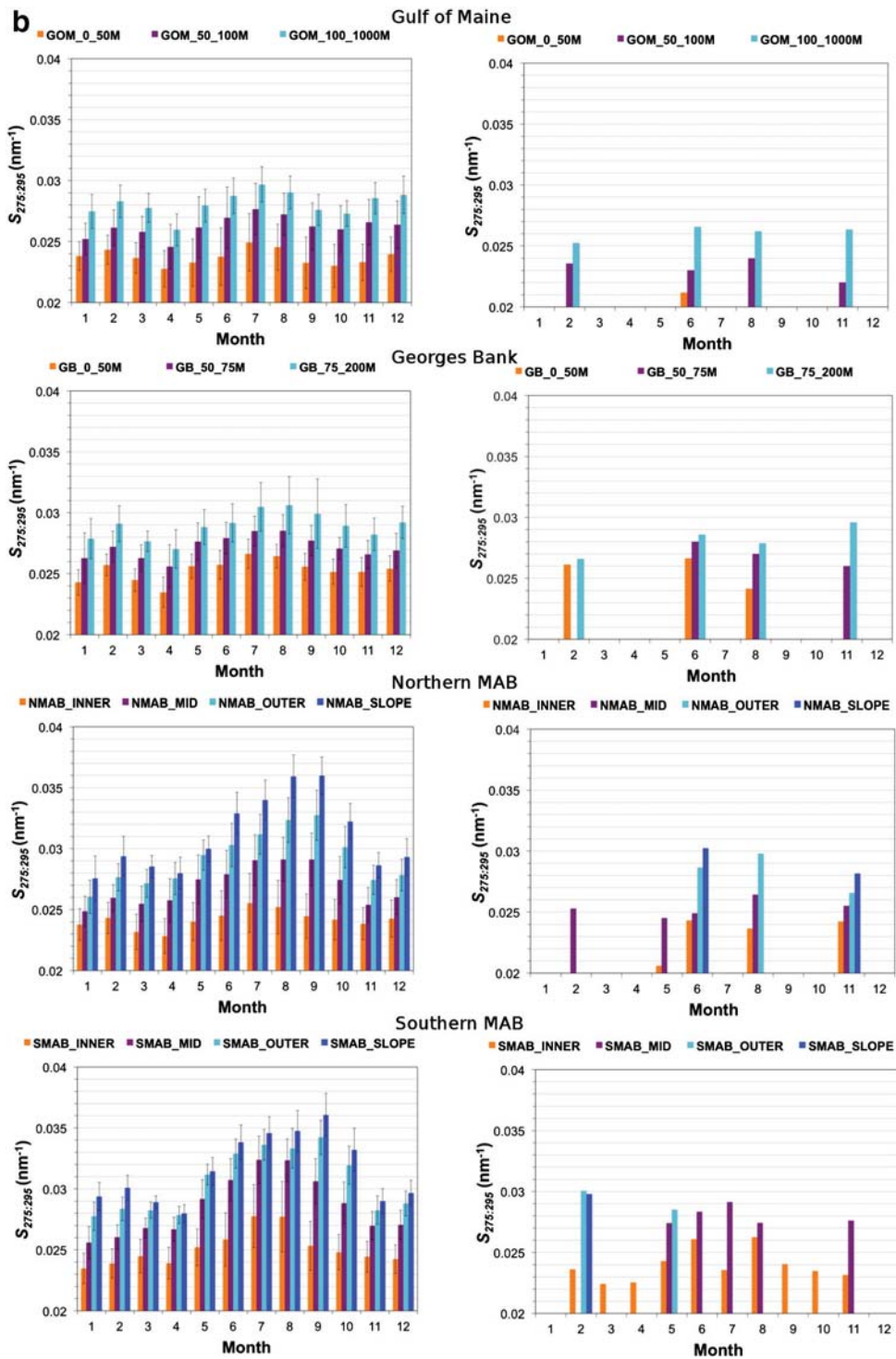
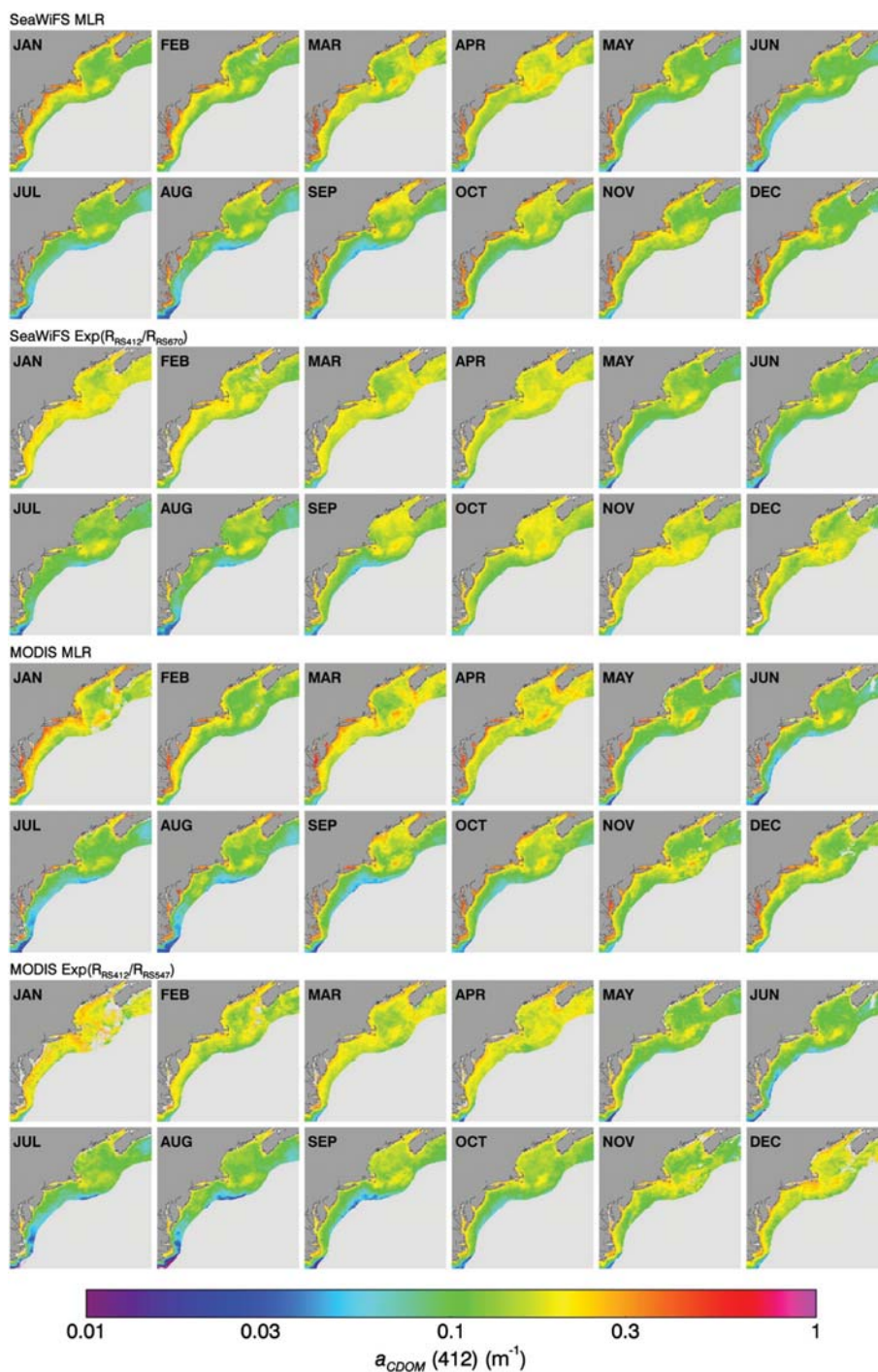


Fig. 10 (continued).

the QAA-based and MLR algorithms for  $S_{275:295}$  and  $S_{300:600}$  compared to field data indicate that the  $S_{275:295}$  and  $S_{300:600}$  MLR algorithms yield better results for these products (Table 2; Figs. 12–13).

The time series analysis from the lower Chesapeake Bay region and monthly composites show that MODIS and SeaWiFS retrievals of  $a_{CDOM}(412)$  and  $S_{275:295}$  using the MLR algorithms compare to within the measured uncertainty of the validation statistics (Figs. 9–10; Table 7). Nevertheless, at a few time points and locations from the lower Chesapeake Bay region time series,  $a_{CDOM}(412)$  field measurements were noticeably higher (and  $S_{275:295}$  values lower)

than the satellite time series trend such as on July 4 (inner shelf), September 6 (bay mouth and plume) and November 28 (bay mouth and plume) of 2006 and April 23, 2007 (inner shelf). On all but the April 23 date, the satellite observations and field sampling occurred from one to many days apart. River discharge into Chesapeake Bay and freshwater outflow at the bay mouth were significantly higher than baseflow in the days and weeks prior to July 4, September 6 and November 28, 2006 (see Fig. 11 in Mannino et al., 2008). This could explain the much higher in situ  $a_{CDOM}(412)$  (and lower  $S_{275:295}$ ) on these dates compared to other sampling periods. The inner shelf sample



**Fig. 11.** Monthly mean satellite-derived  $a_{CDOM}(412)$  from SeaWiFS and MODIS-Aqua for the year 2006 computed with the MLR and band ratio (exponential one-phase decay  $R_{rs}(412)/R_{rs}(670)$  or  $R_{rs}(412)/R_{rs}(547)$ ) algorithms.

from April 23, 2007 was collected  $\sim 1.75$  h and  $\sim 2.5$  h prior to the SeaWiFS and MODIS-Aqua overpasses, respectively, but at the bay mouth site only  $\sim 0.5$  h after the SeaWiFS overpass and  $\sim 1$  min prior to the MODIS overpass. The sensor zenith angle for SeaWiFS ( $\sim 56^\circ$ ) was quite high for the lower Chesapeake Bay region on April 23 resulting in pixel areas of  $\sim 4.2$  km<sup>2</sup> at the inner shelf site and  $\sim 4.4$  km<sup>2</sup> at the bay mouth station, which would likely increase the uncertainty in SeaWiFS retrievals. The measured  $a_{CDOM}(412)$  at the bay mouth site on April 23 was only 20% higher (7.5% higher for  $S_{275:295}$ ) than the MODIS value, which is within the estimated validation uncertainty (Table 7). The sensor zenith angle ( $\sim 11^\circ$ ) for MODIS-Aqua and pixel areas ( $\sim 1.3$  km<sup>2</sup>) were quite modest on this particular date.

#### 4.2. Factors contributing to uncertainty in SeaWiFS and MODIS CDOM and $R_{rs}$ products

SeaWiFS and MODIS  $R_{rs}$  products are validated with in situ matchups within the NES LME to account for the performance of the CDOM algorithms. The  $R_{rs}$  bands in the blue (412 and 443 nm) and red (667, 670 and 678 nm) had higher relative error (MAPD) than the other bands for both SeaWiFS and MODIS (Table 8). Our  $R_{rs}$  matchup results are consistent with previous studies comparing matchups of SeaWiFS and MODIS-Aqua with in situ water-leaving radiances (or  $R_{rs}$ ) within marine coastal waters (e.g., Antoine et al., 2008; Goyens et al., 2013; Werdell, Franz, & Bailey, 2010; Zibordi, Berthon, Mélin, D'Alimonte, & Kaitala,

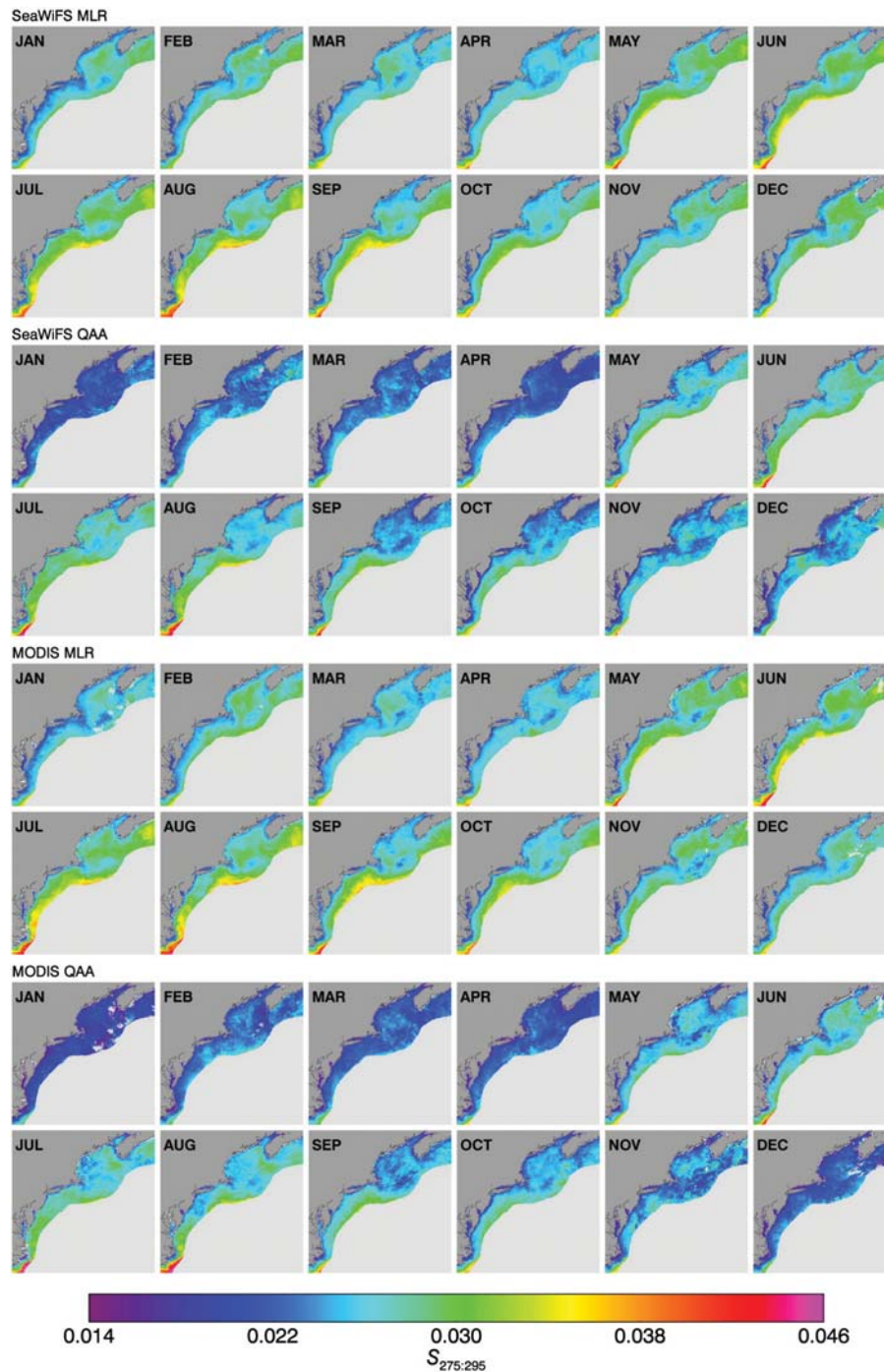


Fig. 12. Monthly mean satellite-derived  $S_{300:600}$  from SeaWiFS and MODIS-Aqua for the year 2006 computed with the MLR and QAA-based algorithms.

2009). These studies and others affirm that MODIS and SeaWiFS  $R_{rs}$  retrievals have higher uncertainties in coastal waters compared to pelagic waters of the global ocean (Bailey & Werdell, 2006).

There are several possible explanations for the discrepancies between satellite and in situ  $R_{rs}$  measurements and derived products: (1) uncertainties in the field-derived measurements (2) in-water constituents and thus optical properties of coastal waters are too complex and variable spatially and temporally for proper satellite-to-in situ comparisons (case 2 waters; IOCCG 2000), (3) imperfect atmospheric correction of the atmospheric properties associated with the scattering and absorption by aerosols and absorption by ozone and nitrogen dioxide ( $\text{NO}_2$ ) and other atmospheric constituents that can occur in higher concentrations on continental margins than the open ocean,

(4) uncertainties in satellite retrievals due to solar illumination and sensor viewing geometry including bidirectional reflectance distribution function (BRDF), (5) uncertainties in the satellite sensor calibration and vicarious calibration, and (6) mismatch in satellite pixel and sample location. All of these factors are likely to impact satellite retrievals of  $R_{rs}$  and CDOM in our study region to varying degrees. The  $R_{rs}$  band ratios do yield improved validation results compared to the individual  $R_{rs}$  bands, particularly for SeaWiFS (Table 8). This suggests some spectrally dependent uncertainties in the satellite and/or field data  $R_{rs}$  bands are removed when one band is divided by another band as observed in prior studies (e.g., Zibordi et al., 2009).

The Spearman rank correlation analyses of the satellite and in situ matchup residuals indicate that certain factors including solar

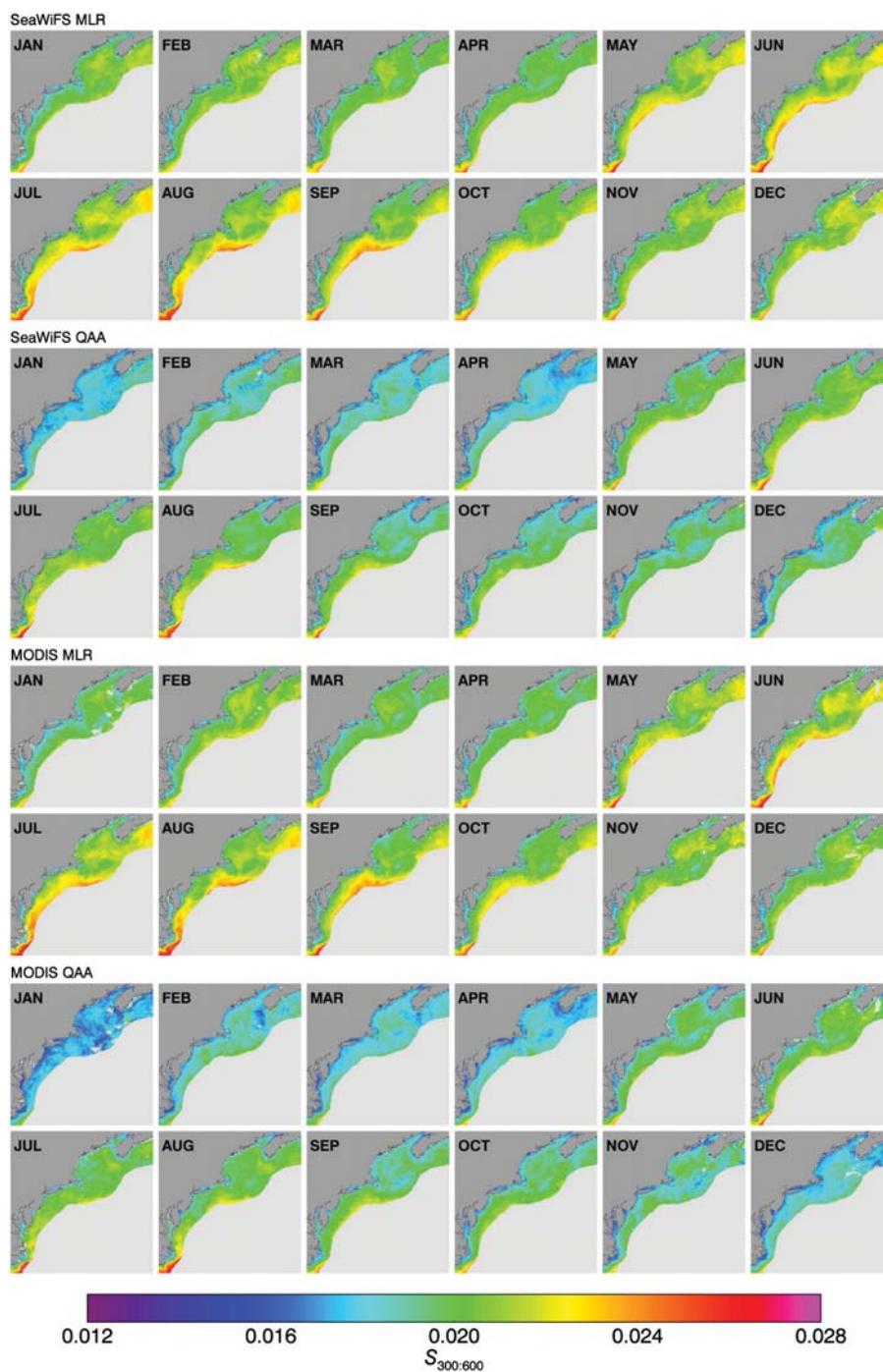


Fig. 13. Monthly mean satellite-derived  $S_{275:295}$  from SeaWiFS and MODIS-Aqua for the year 2006 computed with the MLR and QAA-based algorithms.

illumination, sensor geometry and atmospheric corrections for aerosols and trace gases should be explored further as potential sources of uncertainty in  $R_{rs}$  and the derived satellite products such as CDOM (Tables 9–11). The default BRDF corrections within SeaDAS may not be appropriate for the case 2 waters within our study region (Morel, Antoine, & Gentili, 2002). The SeaDAS default f/Q correction factor was applied in the processing of the SeaWiFS and MODIS data used for this work because our study region spans both case 1 and case 2 waters. The similarity in absorption spectra of CDOM and detrital particles may have an impact on our retrievals of CDOM products in more turbid areas of our study region (Pan et al., 2008). The Spearman correlation

results reveal a significant correlation between residuals of  $a_{CDOM}$  and  $R_{rs}(670)$ , a relative measure of particle load, for SeaWiFS but only for the band ratio and QAA-based algorithms and not for the MLR algorithms or the S products (Table 10). For MODIS, only the  $S_{275:295}$  MLR algorithms have a significant correlation with particle load,  $R_{rs}(645)$  (Table 11). It is noteworthy that the difference in time between the satellite overpass and in situ sample collection and satellite pixel dimensions are not significantly correlated with any of the  $a_{CDOM}(412)$ ,  $S_{275:295}$  and  $S_{300:600}$  residuals. If spatial variability and temporal variability are major factors in satellite retrieval uncertainties for our CDOM products, then this is likely to occur at sub-pixel scales in addition to

spatially variable regions such as riverine and estuarine plumes, fronts and eddies. Additional validation datasets and satellite data analysis would be required to resolve which factors have the greatest effect on satellite  $R_{rs}$  and CDOM product uncertainties.

#### 4.3. Spatial and temporal variability of $a_{CDOM}(412)$ , $S_{275:295}$ and $S_{300:600}$

Satellite-derived distributions of  $a_{CDOM}(412)$ ,  $S_{275:295}$  and  $S_{300:600}$  are spatially and temporally consistent with field measurements (Figs. 9–13; Table 2). Because terrestrial DOM is the main source of CDOM to estuaries and coastal ocean,  $a_{CDOM}(412)$  values should generally decrease from the estuary to the edge of the continental slope, especially during the high river flow periods of January to April (Del Vecchio & Blough, 2004; Mannino et al., 2008) as illustrated in our satellite imagery and field data (Figs. 10a and 11; Table 2). The MLR  $a_{CDOM}(412)$  products are more consistent with our expectations than the band-ratio algorithms, particularly for inner shelf and estuarine regions where  $a_{CDOM}(412)$  should be higher than mid- and outer-shelf regions. In contrast, the band-ratio values are very similar between the lower estuaries and inner- and mid-shelf during the winter–spring period. The decrease in  $a_{CDOM}(412)$  across the shelf from April through August is consistent with solar photo-bleaching of CDOM for this region (Del Vecchio et al., 2009). The increase in surface  $a_{CDOM}(412)$  from early to late autumn corresponds to greater river discharge compared to summer and seasonal mixing of the water column, which introduces non-photo-bleached CDOM into the surface waters from below the mixed layer. SeaWiFS and MODIS distributions of  $S_{275:295}$  and  $S_{300:600}$  are consistent with the general interpretations of  $a_{CDOM}(412)$  distributions that seasonal river discharge of terrestrial DOM, summer photo-bleaching and seasonal stratification and mixing of the water column regulate the seasonal variability of CDOM along the northeastern U.S. (Figs. 10–13). In addition to seasonal changes,  $a_{CDOM}(412)$ ,  $S_{275:295}$  and  $S_{300:600}$  fluctuate quite rapidly on the scale of < 1 h to a few days in coastal waters implying that CDOM could be used to follow dynamic physical processes such as freshwater discharge, coastal currents, upwelling, eddies, storm events, etc. (Fig. 9).

#### 4.4. Potential of UV radiometry bands for satellite retrieval of CDOM properties

Satellite observations from SeaWiFS and MODIS are limited to retrievals of ocean reflectance in the visible and near-infrared wavelength spectrum. Future NASA ocean color satellite sensors such as on the PACE and GEO-CAPE missions are expected to be equipped with UV capability and designed to produce improved satellite retrievals for blue bands such as 412 nm (Pre-aerosol, clouds, and ocean ecosystem (PACE) mission science definition team report, 2012). Other planned sensors such as the Japanese Second Generation Global Imager (SGLI) and Geostationary Ocean Color Imager II (GOCI-II) have planned capabilities to retrieve ocean reflectances in the UV. Since CDOM absorbance is more intense further into the UV in combination with a weaker absorbance, with respect to CDOM, from phytoplankton (pigments) and detrital/non-pigmented particle absorbance from 412 to 350 nm, the addition of UV bands should improve the retrievals of CDOM absorption and separation of CDOM from phytoplankton and detrital particle absorption. For example, prior work has demonstrated the potential for more robust algorithms to retrieve CDOM or CDM with UV  $R_{rs}$  from a band ratio of 325/565 and 340/565 (Tedetti et al., 2010) or with UV  $K_d$  from a band ratio of 320/780 (Hooker, Morrow, & Matsuoka, 2013). Our application of UV  $R_{rs}$  bands shows promise for improved retrievals of  $a_{CDOM}$ ,  $S_{275:295}$  and  $S_{300:600}$  using the UV–MLR with  $R_{rs}(380)$  or  $K_d$ -based algorithms (Tables 5–6). These bio-optical algorithms yield a much better fit to the in situ data with  $R_{rs}(380)$  and  $K_d(340)$  or  $K_d(380)$  through the full range of our  $a_{CDOM}$ ,  $S_{275:295}$  and  $S_{300:600}$  measurements (Figs. 4–5). In addition, UV bands may improve the capability of models that retrieve multiple inherent optical properties (IOP) (Lee et al., 2002; Maritorea

et al., 2002; Tilstone et al., 2012; Werdell et al., 2013) to distinguish between CDOM and detrital particle absorption.

#### 4.5. Implications

Because CDOM is a dominant light-absorbing constituent in the ocean and has absorption spectra that overlap significantly with phytoplankton, detritus and minerals, the impact of CDOM absorption on color-leaving radiances should be considered when applying ocean color remote sensing data to quantify other ocean constituents. Indeed, the overlap in absorption results in substantial uncertainties in satellite retrievals of Chl (e.g., Pan, Mannino, Russ, Hooker, & Harding, 2010; Sauer, Roesler, Werdell, & Barnard, 2012; Siegel, Maritorea, Nelson, & Behrenfeld, 2005; Siegel, Maritorea, Nelson, Behrenfeld, & McClain, 2005; Siegel et al., 2013) using the standard band ratio algorithms (OC4 and OC3 for SeaWiFS and MODIS, respectively; O'Reilly et al., 2000). The capability to retrieve  $a_{CDOM}(\lambda)$  and  $S_{300:600}$  relatively accurately with the MLR algorithms can enable improved retrievals of Chl and potentially other constituents. For portions of our study region where detrital particle absorption is very low or insignificant, which is generally the case for much of the offshore waters of our study region (Pan et al., 2008; Yentsch & Phinney, 1997), existing semi-analytical models (e.g., GSM01; Maritorea et al., 2002) can be modified to incorporate satellite-derived  $a_{CDOM}(\lambda)$  and  $S_{300:600}$  to represent CDM and permit retrieval of Chl (and phytoplankton absorption) at higher accuracy than the standard maximum band ratio algorithms.

SeaWiFS and MODIS sensors lack the capability to retrieve ocean reflectance in the ultraviolet region of the electromagnetic spectrum. Yet, prior work (Fichot et al., 2013; Johannessen et al., 2003; Mannino et al., 2008; Swan, Nelson, & Siegel, 2013) and results presented here demonstrate retrievals of  $a_{CDOM}$  or  $S$  for UV wavelengths. Because of the strong correlation between  $a_{CDOM}(\lambda)$  with  $a_{CDOM}$  at other wavelengths such as  $a_{CDOM}(412)$  (Fig. 8), one can infer information on CDOM in the UV from visible band reflectance. Therefore, we can apply SeaWiFS, MODIS and other ocean color sensors with a similar band set to retrieve  $a_{CDOM}$  and  $S$  at UV wavelengths. One advantage to this is the enormous potential to applying satellite retrievals of  $a_{CDOM}(UV)$ ,  $S_{300:600}$  and  $S_{275:295}$  to retrieving chemical properties of DOM (e.g., Hernes & Benner, 2003; Mannino et al., 2008; Spencer, Aiken, Wickland, Striegl, & Hernes, 2008; Spencer et al., 2010; Spencer, Butler, & Aiken, 2012; Fichot & Benner, 2011; Fichot & Benner, 2012; Fichot et al., 2013).

Since the magnitude of  $a_{CDOM}(\lambda)$  and CDOM spectral slopes depend on its origin and composition, satellite retrievals of CDOM properties in coastal waters can be applied to study relative contributions of different carbon sources, track water masses, quantify distributions and variability of DOC, and estimate photooxidation of DOM. Satellite products of  $a_{CDOM}(\lambda)$  can be applied to retrieve DOC concentrations (e.g., Griffin, Frey, Rogan, & Holmes, 2011; Korosov, Posdnyakov, & Grassl, 2012; Mannino et al., 2008) and quantify processes such as river export of DOC (Del Castillo & Miller, 2008; López, Del Castillo, Miller, Salisbury, & Wisser, 2012), cross-shelf fluxes of DOC, and photochemical production of inorganic carbon (Bélanger et al., 2008; Del Vecchio et al., 2009; Fichot & Miller, 2010). CDOM can be used as a good proxy for tracing physical circulation and water-mass history, tracking freshwater plumes, identifying pollutants and assessing their impact on inland and coastal water quality and ecosystem health.  $S_{300:600}$  can vary with the source of DOM, but  $S_{300:600}$  is also influenced by photochemical and biological processes (see reviews by Blough & Green, 1995; Blough & Del Vecchio, 2002). Since  $S_{300:600}$  generally increases with salinity and decreasing molecular weight and aromatic content (Blough & Del Vecchio, 2002), this suggests that lower  $S_{300:600}$  values represent higher proportions of terrestrial DOM, though there are notable exceptions with respect to the salinity relationship (e.g., Stedmon et al., 2000). Helms et al. (2008) recently introduced  $S_{275:295}$  as a more powerful measure of DOM source, molecular weight

and of photochemical and microbial modifications to CDOM than  $S_{300:600}$ . With validated algorithms for  $a_{CDOM}(\lambda)$ ,  $S_{275:295}$  and  $S_{300:600}$  such as those presented here, it is possible to retrieve other chemical properties of DOM through in situ relationships between  $a_{CDOM}(\lambda)$  or  $S_{275:295}$  and dissolved lignin phenol concentrations (e.g., Hernes & Benner, 2003; Spencer et al., 2008, 2009, 2010, 2012; Osburn & Stedmon, 2011), lignin yields (Fichot & Benner, 2012; Fichot et al., 2013), and dissolved black carbon (e.g., Stubbins, Niggemann, & Dittmar, 2012).

## 5. Conclusions

Several algorithms have been developed and validated for the retrieval of  $a_{CDOM}(\lambda)$ ,  $S_{275:295}$  and  $S_{300:600}$  with SeaWiFS and MODIS-Aqua for the continental margin of the northeastern U.S. The validation metrics and processing of SeaWiFS and MODIS data illustrate that the MLR algorithms provide the optimal retrievals for  $a_{CDOM}(\lambda)$ ,  $S_{300:600}$  and  $S_{275:295}$ . The relative errors (MAPD) for the validated CDOM products fall within the uncertainty requirements of 35% for satellite retrieval of open ocean chlorophyll-*a* (McClain, 2009). The MAPD for  $a_{CDOM}(\lambda)$  algorithms range from ~24% to 30% and from 6% to 10% for the  $S_{275:295}$  and  $S_{300:600}$  products, respectively. Algorithms developed and evaluated with in situ measurements employing  $R_{rs}$  bands in the ultraviolet produce better fits to the in situ data than the algorithms with only visible wavelength  $R_{rs}$  bands. The algorithms with UV bands will enable improved retrievals of  $a_{CDOM}(\lambda)$ ,  $S_{275:295}$  and  $S_{300:600}$  from future satellite sensors with UV measurement capabilities. The correlation analyses of the validation residuals for the CDOM products and  $R_{rs}$  suggest that several factors should be explored further to understand and possibly diminish the uncertainty in satellite retrievals within the coastal ocean, including solar zenith angle, sensor viewing angle, atmospheric products applied for atmospheric corrections, as well as

the in situ spatial and temporal heterogeneity of  $a_{CDOM}$  and other optical properties.

## Acknowledgments

Various NASA programs supported the work described in this publication including the Ocean Biology and Biogeochemistry Program (Climate Variability of the East Coast [ClIVEC] project and calibration/validation project), Biodiversity Program, New Investigator Program and Interdisciplinary Science. We thank the captains and crews of the R/V Delaware II, R/V Sharp, R/V Gulf Challenger, R/V Connecticut, and R/V Fay Slover. Our profound gratitude to Jerry Prezioso, Jon Hare, and Harvey Walsh for accommodating our ClIVEC project research on NOAA's Northeast Marine Fisheries Service Ecosystem Monitoring (ECO-Mon) cruises. Many thanks to Veronica Lance, Xiaoju Pan, Davide D'Alimonte, Mary Russ, Katherine Filippino, Peter Bernhardt, Jean-Noel Druon, and John Morrow for their assistance on the various research cruises that contributed to this work. We thank Mike Twardowski for organizing and leading the OBB-supported calibration/validation project and cruises in the Hudson River-Estuary and New York Bight region. Ru Morrison kindly invited our group to participate on cruises in the Gulf of Maine and waters surrounding the Martha's Vineyard Coastal Observatory. Thanks to Jay Austin, Eileen Hofmann and John Klinck for planning and/or assistance with the Old Dominion University Chesapeake Bay mouth hydrography transects and data access. We express our sincere gratitude to Chuck McClain and three anonymous reviewers for providing insightful comments on a prior draft of this manuscript that improved the final version of this manuscript. Many thanks to the NASA Goddard Space Flight Center Ocean Biology Processing Group for their efforts in providing high quality MODIS and SeaWiFS satellite data products.

## Appendix A

**Table A1**

Coefficients and goodness of fit parameters for band-ratio bio-optical  $a_{CDOM}$  algorithms developed from field observations of  $a_{CDOM}(\lambda)$  and remote sensing reflectance ( $R_{rs}(\lambda)$ ). See Table 2 for details.

Exponential one-phase decay equation	$a_{CDOM275}$	$a_{CDOM355}$	$a_{CDOM380}$	$a_{CDOM412}$	$a_{CDOM443}$
$X = \ln[(Y - B_0) / B_2] / -B_1$	$B_0 = 0.2581$	0.2452	0.2492	0.2487	0.2479
$Y = R_{rs}(412) / R_{rs}(555)$	$B_1 = 1.583$	5.576	8.689	14.028	23.40
$X = a_{CDOM}(\lambda)$	$B_2 = 24.87$	4.838	4.608	4.085	3.770
$R^2$	0.881	0.942	0.948	0.950	0.937
Sy.x	0.113	0.086	0.081	0.0806	0.084
n	142	151	152	153	149
Minimum band ratio	0.31	0.295	0.295	0.295	0.295
$X = \ln[(Y - B_0) / B_2] / -B_1$	$B_0 = 0.9925$	0.8569	0.865	0.8625	0.8502
$Y = R_{rs}(412) / R_{rs}(667)$	$B_1 = 2.054$	7.661	11.55	18.44	30.53
$X = a_{CDOM}(\lambda)$	$B_2 = 634.2$	91.97	79.16	62.89	54.78
$R^2$	0.845	0.955	0.959	0.943	0.938
Sy.x	1.046	0.720	0.694	0.736	0.788
n	139	144	145	147	146
Minimum band ratio	1.29	1.1	1.1	1.1	1.1

**Table A2**

Satellite validation statistics of CDOM exponential decay band ratio algorithms for SeaWiFS and MODIS-Aqua.

Product	Algorithm	MAPD	$\pm$ sd	RMSE	Median ratio	SIQR	%Bias	Slope	$R^2$	n
$a_{CDOM275}$	Exp_ $R_{rs}(412)/R_{rs}(555)$	24.8	22.3	1.77	0.88	0.209	-27.3	0.202	0.45	41
$a_{CDOM355}$	Exp_ $R_{rs}(412)/R_{rs}(555)$	32.5	22.0	0.348	0.73	0.222	-34.9	0.282	0.49	41
$a_{CDOM380}$	Exp_ $R_{rs}(412)/R_{rs}(555)$	33.3	21.5	0.224	0.68	0.206	-36.4	0.289	0.50	41
$a_{CDOM412}$	Exp_ $R_{rs}(412)/R_{rs}(555)$	35.6	20.3	0.130	0.62	0.199	-37.6	0.313	0.51	41
$a_{CDOM443}$	Exp_ $R_{rs}(412)/R_{rs}(555)$	36.6	20.3	0.0746	0.61	0.205	-38.1	0.328	0.52	41
$a_{CDOM275}$	Exp_ $R_{rs}(412)/R_{rs}(667)$	28.7	22.8	1.036	1.16	0.176	6.6	0.287	0.24	46
$a_{CDOM355}$	Exp_ $R_{rs}(412)/R_{rs}(667)$	31.6	25.0	0.196	1.20	0.219	4.9	0.350	0.35	46
$a_{CDOM380}$	Exp_ $R_{rs}(412)/R_{rs}(667)$	29.6	23.0	0.122	1.17	0.216	3.2	0.378	0.37	46
$a_{CDOM412}$	Exp_ $R_{rs}(412)/R_{rs}(667)$	27.6	18.2	0.0683	1.14	0.225	0.19	0.429	0.41	46
$a_{CDOM443}$	Exp_ $R_{rs}(412)/R_{rs}(667)$	27.8	17.6	0.0391	1.13	0.227	0.16	0.448	0.41	46

## References

- Andrew, A. A., Del Vecchio, R., Subramaniam, A., & Blough, N. V. (2013). Chromophoric dissolved organic matter (CDOM) in the equatorial Atlantic Ocean: Optical properties and their relation to CDOM structure and source. *Marine Chemistry*, 148, 33–43.
- Antoine, D., d'Ortenzio, F., Hooker, S. B., Bécuc, G., Gentili, B., Tailliez, D., et al. (2008). Assessment of uncertainty in the ocean reflectance determined by three satellite ocean color sensors (MERIS, SeaWiFS and MODIS-A) at an offshore site in the Mediterranean Sea (BOUSSOLE project). *Journal of Geophysical Research*, 113, C07013. <http://dx.doi.org/10.1029/2007JC004472>.
- Antoine, D., Hooker, S. B., Bélanger, S., Matsuoka, A., & Babin, M. (2013). Apparent optical properties of the Canadian Beaufort Sea, part I: Observational overview and water column relationships. *Biogeosciences*, 10, 4493–4509.
- Aurin, D. A., & Dierssen, H. M. (2012). Advantages and limitations of ocean color remote sensing in CDOM-dominated, mineral-rich coastal and estuarine waters. *Remote Sensing of Environment*, 125, 181–197.
- Bailey, S. W., & Werdell, P. J. (2006). A multi-sensor approach for the on-orbit validation of ocean color satellite data products. *Remote Sensing of Environment*, 102, 12–23.
- Bélanger, S., Babin, M., & Larouche, P. (2008). An empirical ocean color algorithm for estimating the contribution of chromophoric dissolved organic matter to total light absorption in optically complex waters. *Journal of Geophysical Research*, 113, C04027. <http://dx.doi.org/10.1029/2007JC004436>.
- Benner, R. (2002). Chemical composition and reactivity. In D. A. Hansell, & C. A. Carlson (Eds.), *Biogeochemistry of marine dissolved organic matter* (pp. 59–90). San Diego, CA: Academic Press.
- Blough, N. V., & Del Vecchio, R. (2002). Chromophoric DOM in the coastal environment, in biogeochemistry of marine dissolved organic matter. In D. A. Hansell, & C. A. Carlson (Eds.), *Biogeochemistry of marine dissolved organic matter* (pp. 509–546). San Diego, CA: Academic Press.
- Blough, N. V., & Green, S. (1995). The use of in situ and airborne fluorescence measurements to determine UV absorption coefficients and DOC concentrations in surface waters. *Limnology & Oceanography*, 40, 411–415.
- Bricaud, A., Ciotti, A.M., & Gentili, B. (2012). Spatial-temporal variations in phytoplankton size and colored detrital matter absorption at global and regional scales, as derived from twelve years of SeaWiFS data (1998–2009). *Global Biogeochemical Cycles*, 26, GB1010. <http://dx.doi.org/10.1029/2010GB003952>.
- Bricaud, A., Morel, A., & Prieur, L. (1981). Absorption by dissolved organic matter of the sea (yellow substance) in the UV and visible domains. *Limnology & Oceanography*, 26, 43–53.
- Brown, C. A., Huot, Y., Werdell, P. J., Gentili, B., & Claustre, H. (2008). The origin and global distribution of second order variability in satellite ocean color and its potential applications to algorithm development. *Remote Sensing of Environment*, 112, 4186–4203.
- Carder, K. L., Chen, F. R., Lee, Z. P., Hawes, S. K., & Kamykowski, D. (1999). Semianalytical moderate-resolution imaging spectrometer algorithms for chlorophyll and absorption with bio-optical domains based on nitrate-depletion temperatures. *Journal of Geophysical Research*, 104(C3), 5403–5421.
- Carder, K. L., Hawes, S. K., Baker, K. A., Smith, R. C., Steward, R. G., & Mitchell, B. G. (1991). Reflectance model for quantifying chlorophyll a in the presence of productivity degradation products. *Journal of Geophysical Research*, 96(C11), 20599–20611.
- D'Sa, E. J., & Miller, R. L. (2003). Bio-optical properties in waters influenced by the Mississippi River during low flow conditions. *Remote Sensing of Environment*, 84, 538–549.
- D'Sa, E. J., Miller, R. L., & Del Castillo, C. E. (2006). Bio-optical properties and ocean color algorithms for coastal waters influenced by the Mississippi River during a cold front. *Applied Optics*, 45, 7410–7428.
- Del Castillo, C. E., Coble, P. G., Morell, J. M., López, J. M., & Corredor, J. E. (1999). Analysis of the optical properties of the Orinoco River plume by absorption and fluorescence spectroscopy. *Marine Chemistry*, 66, 35–51.
- Del Castillo, C. E., & Miller, R. L. (2008). On the use of ocean color remote sensing to measure the transport of dissolved organic carbon by the Mississippi River Plume. *Remote Sensing of Environment*, 112, 836–844.
- Del Vecchio, R., & Blough, N. V. (2004). Spatial and seasonal distribution of chromophoric dissolved organic matter (CDOM) and dissolved organic carbon (DOC) in the Middle Atlantic Bight. *Marine Chemistry*, 89, 169–187.
- Del Vecchio, R., & Subramaniam, A. (2004). Influence of the Amazon River on the surface optical properties of the western tropical North Atlantic Ocean. *Journal of Geophysical Research*, 109, C11001. <http://dx.doi.org/10.1029/2004JC002503>.
- Del Vecchio, R., Subramaniam, A., Uz, S. S., Ballabrera-Poy, J., Brown, C. W., & Blough, N. V. (2009). Decadal time-series of SeaWiFS retrieved CDOM absorption and estimated CO<sub>2</sub> photoproduction on the continental shelf of the eastern United States. *Geophysical Research Letters*, 36, L02602. <http://dx.doi.org/10.1029/2008GL036169>.
- Doerffer, R., & Schiller, H. (2007). The MERIS case 2 water algorithm. *International Journal of Remote Sensing*, 28, 517–535.
- Dong, Q., Shang, S., & Lee, Z. (2013). An algorithm to retrieve absorption coefficient of chromophoric dissolved organic matter from ocean color. *Remote Sensing of Environment*, 128, 259–267.
- Ferrari, G. M., Dowell, M.D., Grossi, S., & Targa, C. (1996). Relationship between the optical properties of chromophoric dissolved organic matter and total concentrations of dissolved organic carbon in the southern Baltic Sea region. *Marine Chemistry*, 55, 299–316.
- Fichot, C. G., & Benner, R. (2011). A novel method to estimate DOC concentrations from CDOM absorption coefficients in coastal waters. *Geophysical Research Letters*, 38, L03610. <http://dx.doi.org/10.1029/2010GL046152>.
- Fichot, C. G., & Benner, R. (2012). The spectral slope coefficient of chromophoric dissolved organic matter ( $S_{275-295}$ ) as a tracer of terrigenous dissolved organic carbon in river-influenced ocean margins. *Limnology & Oceanography*, 57, 1453–1466.
- Fichot, C. G., Kaiser, K., Hooker, S. B., Amon, R. M. W., Babin, M., Bélanger, S., et al. (2013). Pan-Arctic distributions of continental runoff in the Arctic Ocean. *Scientific Reports*, 3, 1053. <http://dx.doi.org/10.1038/srep01053>.
- Fichot, C. G., & Miller, W. L. (2010). An approach to quantify depth-resolved marine photochemical fluxes using remote sensing: Application to carbon monoxide (CO) photoproduction. *Remote Sensing of Environment*, 114, 1363–1377.
- Chapter 2. Field, C. B., Sarmiento, J., & Hales, B. (2007). The carbon cycle of North America in a global context. In A. W. King, L. Dilling, G. P. Zimmerman, D.M. Fairman, R. A. Houghton, G. Marland, A. Z. Rose, & T. J. Wilbanks (Eds.), *The First State of the Carbon Cycle Report (SOCCR): The North American Carbon Budget and Implications for the Global Carbon Cycle (21–28). A Report by the U.S. Climate Change Science Program and the Subcommittee on Global Change Research*. Asheville, NC: National Oceanic and Atmospheric Administration, National Climatic Data Center.
- Goyens, C., Jamet, C., & Schroeder, T. (2013). Evaluation of four atmospheric correction algorithms for MODIS-Aqua images over contrasted coastal waters. *Remote Sensing of Environment*, 131, 63–75.
- Griffin, C. G., Frey, K. E., Rogan, J., & Holmes, R. M. (2011). Spatial and interannual variability of dissolved organic matter in the Kolyma River, East Siberia, observed using satellite imagery. *Journal of Geophysical Research*, 116, G03018. <http://dx.doi.org/10.1029/2010JG001634>.
- Hedges, J. I. (2002). Why dissolved organic matter, in biogeochemistry of marine dissolved organic matter. In D. A. Hansell, & C. A. Carlson (Eds.), *Biogeochemistry of marine dissolved organic matter* (pp. 1–33). San Diego, CA: Academic Press.
- Helm, J. R., Stubbins, A., Ritchie, J.D., Minor, E. C., Kieber, D. J., & Mopper, K. (2008). Absorption spectral slopes and slope ratios as indicators of molecular weight, source, and photobleaching of chromophoric dissolved organic matter. *Limnology & Oceanography*, 53, 955–969.
- Hernes, P. J., & Benner, R. (2003). Photochemical and microbial degradation of dissolved lignin phenols: Implications for the fate of terrigenous dissolved organic matter in marine environments. *Journal of Geophysical Research*, 108(C9), 3291. <http://dx.doi.org/10.1029/2002JC001421>.
- Hoge, F. E., & Lyon, P. E. (2002). Satellite observation of chromophoric dissolved organic matter (CDOM) variability in the wake of hurricanes and typhoons. *Geophysical Research Letters*, 29, 1908. <http://dx.doi.org/10.1029/2002GL015114>.
- Hoge, F. E., Wright, C. W., Lyon, P. E., Swift, R. N., & Yungel, J. K. (2001). Inherent optical properties imagery of the western North Atlantic Ocean: Horizontal spatial variability of the upper mixed layer. *Journal of Geophysical Research*, 106(C12), 31,129–31,138.
- Hooker, S. B., Lind, R. N., Morrow, J. H., & Brown, J. W. (2010). The submersible biospherical optical profiling system (SuBOPS). In J. H. Morrow, S. B. Hooker, C. R. Booth, G. Bernhard, R. N. Lind, & J. W. Brown (Eds.), *Advances in measuring the apparent optical properties (AOPs) of optically complex waters* (pp. 17–26). Greenbelt, Maryland: NASA Goddard Space Flight Center (NASA TM/2010–215856).
- Hooker, S. B., Morrow, J. H., & Matsuoka, A. (2013). Apparent optical properties of the Canadian Beaufort Sea, part II: The 1% and 1 cm perspective in deriving and validating AOP data products. *Biogeosciences*, 10, 4511–4527.
- Hooker, S. B., Zibordi, G., Berthon, J. -F., D'Alimonte, D., Maritorea, S., McLean, S., et al. (2001). Results of the second SeaWiFS data analysis round robin, March 2000 (DARR-00). In S. B. Hooker, & E. R. Firestone (Eds.), *NASA TM 2001–206892, 15*. Greenbelt, Maryland: NASA Goddard Space Flight Center (71 pp.).
- Johannessen, S.C., Miller, W. L., & Cullen, J. J. (2003). Calculation of UV attenuation and colored dissolved organic matter absorption spectra from measurements of ocean color. *Journal of Geophysical Research*, 108(C9), 3301–3313.
- Joint Global Ocean Flux Study (1991). *JGOFS core measurements protocols*. JGOFS Report No. 6, Scientific Committee on Oceanic Research (40 pp.).
- Kahru, M., & Mitchell, B. G. (2001). Seasonal and nonseasonal variability of satellite-derived chlorophyll and colored dissolved organic matter concentration in the California current. *Journal of Geophysical Research*, 106, 2517–2529.
- Korosov, A. A., Posodnyakov, D.V., & Grassl, H. (2012). Spaceborne quantitative assessment of dissolved organic carbon fluxes in the Kara Sea. *Advances in Space Research*, 50, 1173–1188.
- Lee, Z. P., Arnone, R. A., Hu, C., Werdell, P. J., & Lubac, B. (2010). Uncertainties of optical parameters and their propagations in an analytical ocean color inversion algorithm. *Applied Optics*, 49, 369–381.
- Lee, Z. P., Carder, K. L., & Arnone, R. A. (2002). Deriving inherent optical properties from water color: A multiband quasi-analytical algorithm for optically deep waters. *Applied Optics*, 41, 5755–5772.
- Loiselle, S. A., Bracchini, L., Dattilo, A.M., Ricci, M., Tognazzi, A., Cózar, A., et al. (2009). Optical characterization of chromophoric dissolved organic matter using wavelength distribution of absorption spectral slopes. *Limnology and Oceanography*, 54, 590–597.
- López, R., Del Castillo, C. E., Miller, R. L., Salisbury, J., & Wisser, D. (2012). Examining organic carbon transport by the Orinoco River using SeaWiFS imagery. *Journal of Geophysical Research*, 117. <http://dx.doi.org/10.1029/2012JG001986> G03022.
- Magnuson, A., Harding, L. W., Jr., Mallonee, M. E., & Adolf, J. (2004). Bio-optical model for Chesapeake Bay and the Middle Atlantic Bight. *Estuarine, Coastal and Shelf Science*, 61, 403–424.
- Mannino, A., Russ, M. E., & Hooker, S. B. (2008). Algorithm development and validation for satellite-derived distributions of DOC and CDOM in the U.S. Middle Atlantic Bight. *Journal of Geophysical Research*, 113, C07051. <http://dx.doi.org/10.1029/2007JC004493>.
- Maritorea, S., Siegel, D. A., & Peterson, A.R. (2002). Optimization of a semianalytical ocean color model for global-scale applications. *Applied Optics*, 41, 2705–2714.
- Matsuoka, A., Hooker, S. B., Bricaud, A., Gentili, B., & Babin, M. (2013). Estimating absorption coefficients of colored dissolved organic matter (CDOM) using a semi-analytical algorithm for southern Beaufort Sea waters: Application to deriving concentrations of dissolved organic carbon from space. *Biogeosciences*, 10, 917–927.

- McClain, C. R. (2009). A decade of satellite ocean color observation. *Annual Review of Marine Science*, 1, 19–42.
- Miller, W. L., & Zepp, R. G. (1995). Photochemical production of dissolved inorganic carbon from terrestrial organic matter: Significance to the oceanic organic carbon cycle. *Geophysical Research Letters*, 22, 417–420.
- Mitchell, B. G., Kahru, M., Wieland, J., & Stramska, M. (2003). Determination of spectral absorption coefficients of particles, dissolved material and phytoplankton for discrete water samples. In G. S. Fargion, J. L. Mueller, & C. R. McClain (Eds.), *Ocean optics protocols for satellite ocean color sensor validation* (pp. 39–64). Greenbelt, Maryland: NASA Goddard Space Flight Center (NASA/TM-2003-211621/Rev4-Vol.IV).
- Mitchell, B. G., et al. (2000). Determination of spectral absorption coefficients of particles, dissolved material and phytoplankton for discrete water samples. In G. S. Fargion, & J. L. Mueller (Eds.), *Ocean optics protocols for satellite ocean color sensor validation* (pp. 125–153). Greenbelt, Maryland: NASA Goddard Space Flight Center (NASA/TM-2000-209966).
- Mobley, C. D. (1999). Estimation of the remote-sensing reflectance from above-surface measurements. *Applied Optics*, 38, 7442–7455.
- Morel, A., Antoine, D., & Gentili, B. (2002). Bidirectional reflectance of oceanic waters: Accounting for Raman emission and varying particle scattering phase function. *Applied Optics*, 41, 6289–6306.
- Morel, A., & Gentili, B. (2009). A simple band ratio technique to quantify the colored dissolved and detrital organic material from ocean color remotely sensed data. *Remote Sensing of Environment*, 113, 998–1011.
- Mueller, J. L. (2000). Overview of measurement and data analysis protocols. In G. S. Fargion, & J. L. Mueller (Eds.), *Ocean optics protocols for satellite ocean color sensor validation revision 2* (pp. 87–97). Greenbelt, Maryland: NASA Goddard Space Flight Center (NASA TM/2000-209966).
- Mueller, J. L. (2002). Overview of measurement and data analysis methods. In J. L. Mueller, & G. S. Fargion (Eds.), *Ocean optics protocols for satellite ocean color sensor validation* (pp. 123–137). Greenbelt, Maryland: NASA Goddard Space Flight Center (NASA Tech. Memo. 2002-210004/Rev3-Vol.1).
- Mueller, J. L. (2003). Overview of measurement and data analysis methods. In J. L. Mueller, & G. S. Fargion (Eds.), *Ocean optics protocols for satellite ocean color sensor validation* (pp. 1–20). Greenbelt, Maryland: NASA Goddard Space Flight Center (NASA TM 2003-211621/Rev4-Vol.III).
- Mueller, J. L., & Austin, R. W. (1992). Ocean optics protocols for SeaWiFS validation. In S. B. Hooker, & E. R. Firestone (Eds.), *NASA TM 104566. Vol. 5*. Greenbelt, Maryland: NASA Goddard Space Flight Center (43 pp.).
- Mueller, J. L., & Austin, R. W. (1995). Ocean optics protocols for SeaWiFS validation. In S. B. Hooker, E. R. Firestone, & J. G. Acker (Eds.), *NASA TM 104566. Vol. 25*. Greenbelt, Maryland: NASA Goddard Space Flight Center (66 pp.).
- Naik, P., D'Sa, E. J., Grippo, A., Condrey, R., & Fleeger, J. (2011). Absorption properties of shoal dominated waters in the Atchafalaya Shelf, Louisiana, USA. *International Journal of Remote Sensing*, 32, 4383–4406.
- Nelson, N.B., & Siegel, D. A. (2002). Chromophoric DOM in the open ocean. In D. A. Hansell, & C. A. Carlson (Eds.), *Biogeochemistry of marine dissolved organic matter* (pp. 547–578). San Diego, CA: Academic Press.
- Nelson, N.B., & Siegel, D. A. (2013). The global distribution and dynamics of chromophoric dissolved organic matter. *Annual Review in Marine Science*, 5, 447–476.
- Nelson, N.B., Siegel, D. A., Carlson, C. A., & Swan, C. M. (2010). Tracing global biogeochemical cycles and meridional overturning circulation using chromophoric dissolved organic matter. *Geophysical Research Letters*, 37. <http://dx.doi.org/10.1029/2009GL042325> (L03610).
- O'Reilly, J. E., Maritorena, S., O'Brien, M. C., Siegel, D. A., Toole, D., Menzies, D., et al. (2000). SeaWiFS postlaunch calibration and validation analyses, part 3. 49 pp. In S. B. Hooker, & E. R. Firestone (Eds.), *SeaWiFS project postlaunch technical report series. NASA Tech. Memo., Vol. 11.* (pp. 2000-206892). NASA Goddard Space Flight Center.
- Osburn, C. I., & Stedmon, C. A. (2011). Linking the chemical and optical properties of dissolved organic matter in the Baltic–North Sea transition zone to differentiate three allochthonous inputs. *Marine Chemistry*, 126, 281–294.
- Pan, X., Mannino, A., Russ, M. E., & Hooker, S. B. (2008). Remote sensing of the absorption coefficients and chlorophyll a concentration in the U.S. southern Middle Atlantic Bight from SeaWiFS and MODIS-Aqua. *Journal of Geophysical Research*, 113, C11022. <http://dx.doi.org/10.1029/2008JC004852>.
- Pan, X., Mannino, A., Russ, M. E., Hooker, S. B., & Harding, L. W., Jr. (2010). Remote sensing of phytoplankton pigment distribution in the United States northeast coast. *Remote Sensing of Environment*, 114, 2403–2416.
- Pre-aerosol, clouds, and ocean ecosystem (PACE) mission science definition team report. [http://decadal.gsfc.nasa.gov/pace\\_documentation/PACE\\_SDT\\_Report\\_final.pdf](http://decadal.gsfc.nasa.gov/pace_documentation/PACE_SDT_Report_final.pdf). (2012).
- Rochelle-Newall, E. J., & Fisher, T. R. (2002). Chromophoric dissolved organic matter and dissolved organic carbon in Chesapeake Bay. *Marine Chemistry*, 77, 23–41.
- Sauer, M. J., Roesler, C. S., Werdell, P. J., & Barnard, A. (2012). Under the hood of satellite empirical chlorophyll a algorithms: Revealing the dependencies of maximum band ratio algorithms on inherent optical properties. *Optics Express*, 20, 20920–20933.
- Shanmugam, P. (2011). New models for retrieving and partitioning the colored dissolved organic matter in the global ocean: Implications for remote sensing. *Remote Sensing of Environment*, 115, 1501–1521.
- Siegel, D. A., Behrenfeld, M. J., Maritorena, S., McClain, C. R., Antoine, D., Bailey, S. W., et al. (2013). Regional to global assessments of phytoplankton dynamics from the SeaWiFS mission. *Remote Sensing of Environment*, 135, 77–91.
- Siegel, D. A., Maritorena, S., Nelson, N.B., & Behrenfeld, M. J. (2005). Independence and interdependencies among global ocean color properties: Reassessing the bio-optical assumption. *Journal of Geophysical Research*, 110, C07011. <http://dx.doi.org/10.1029/2004JC002527>.
- Siegel, D. A., Maritorena, S., Nelson, N.B., Behrenfeld, M. J., & McClain, C. R. (2005). Colored dissolved organic matter and its influence on the satellite-based characterization of the ocean biosphere. *Geophysical Research Letters*, 32, L20605. <http://dx.doi.org/10.1029/2005GL024310>.
- Siegel, D. A., Maritorena, S., Nelson, N.B., Hansell, D. A., & Lorenzi-Kayser, M. (2002). Global distribution and dynamics of colored dissolved and detrital organic materials. *Journal of Geophysical Research*, 107(C12), 3228. <http://dx.doi.org/10.1029/2001JC000965>.
- Smith, R. C., & Baker, K. S. (1984). The analysis of ocean optical data. In M. Blizard (Ed.), *Ocean optics VII, SPIE*. 478. (pp. 119–126).
- Spencer, R. G. M., Aiken, G. R., Butler, K. D., Dornblaser, M. M., Striegl, R. G., & Hernes, P. J. (2009). Utilizing chromophoric dissolved organic matter measurements to derive export and reactivity of dissolved organic carbon exported to the Arctic Ocean: A case study of the Yukon River, Alaska. *Geophysical Research Letters*, 36, L06401. <http://dx.doi.org/10.1029/2008GL036831>.
- Spencer, R. G. M., Aiken, G. R., Wickland, K. P., Striegl, R. G., & Hernes, P. J. (2008). Seasonal and spatial variability in dissolved organic matter quantity and composition from the Yukon River basin, Alaska. *Global Biogeochemical Cycles*, 22, GB4002. <http://dx.doi.org/10.1029/2008GB003231>.
- Spencer, R. G. M., Butler, K. D., & Aiken, G. R. (2012). Dissolved organic carbon and chromophoric dissolved organic matter properties of rivers in the U.S.A. *Journal of Geophysical Research*, 117, G03001. <http://dx.doi.org/10.1029/2011JG001928>.
- Spencer, R. G. M., Hernes, P. J., Ruf, R., Baker, A., Dyda, R. Y., Stubbins, A., et al. (2010). Temporal controls on dissolved organic matter and lignin biogeochemistry in a pristine tropical river, Democratic Republic of Congo. *Journal of Geophysical Research*, 115, G03013. <http://dx.doi.org/10.1029/2009JG001180>.
- Stedmon, C. A., Markager, S., & Kaas, H. (2000). Optical properties and signatures of chromophoric dissolved organic matter (CDOM) in Danish coastal waters. *Estuarine, Coastal and Shelf Science*, 51, 267–278. <http://dx.doi.org/10.1006/ecss.2000.0645>.
- Stedmon, C. A., Osburn, C. L., & Gragh, T. (2010). Tracing water mass mixing in the Baltic–North Sea transition zone using the optical properties of coloured dissolved organic matter. *Estuarine, Coastal and Shelf Science*, 87, 156–162.
- Steinberg, D. K., Nelson, N., Carlson, C. A., & Prusak, A.C. (2004). Production of chromophoric dissolved organic matter (CDOM) in the open ocean by zooplankton and the colonial cyanobacterium *Trichodesmium* spp. *Marine Ecological Progress Series*, 267, 45–56.
- Stubbins, A., Niggemann, J., & Dittmar, T. (2012). Photo-lability of deep ocean dissolved black carbon. *Biogeosciences*, 9, 1661–1670. <http://dx.doi.org/10.5194/bg-9-1661-2012>.
- Swan, C. M., Nelson, N.B., & Siegel, D. A. (2013). A model for remote estimation of ultraviolet absorption by chromophoric dissolved organic matter based on the global distribution of spectral slope. *Remote Sensing of Environment*, 136, 277–285.
- Swan, C. M., Siegel, D. A., Nelson, N.B., Carlson, C. A., & Nasir, E. (2009). Biogeochemical and hydrographic controls on chromophoric dissolved organic matter distribution in the Pacific Ocean. *Deep-Sea Research I*, 56, 2175–2192.
- Tedetti, M., Charrière, B., Bricaud, A., Para, J., Raimbault, P., & Sempéré, R. (2010). Distribution of normalized water-leaving radiances at UV and visible wave bands in relation with chlorophyll a and colored detrital matter content in the southeast Pacific. *Journal of Geophysical Research*, 115, C02010. <http://dx.doi.org/10.1029/2009JC005289>.
- Tilstone, G. H., Peters, S. W. M., van der Woerd, H. J., Eleveld, M.A., Ruddick, K., Schönfeld, W., et al. (2012). Variability in specific-absorption properties and their use in a semi-analytical ocean colour algorithm for MERIS in north sea and western English channel coastal waters. *Remote Sensing of Environment*, 118, 320–338.
- Tiwari, S. P., & Shanmugam, P. (2011). An optical model for the remote sensing of coloured dissolved organic matter in coastal/ocean waters. *Estuarine, Coastal and Shelf Science*, 93, 396–402.
- Vodacek, A., Blough, N.B., DeGrandpre, M.D., Peltzer, E. T., & Nelson, R. K. (1997). Seasonal variation of CDOM and DOC in the Middle Atlantic Bight: Terrestrial inputs and photooxidation. *Limnology & Oceanography*, 42, 674–686.
- Werdell, P. J., Franz, B.A., & Bailey, S. W. (2010). Evaluation of shortwave infrared atmospheric correction for ocean color remote sensing of Chesapeake Bay. *Remote Sensing of Environment*, 114, 2238–2247.
- Werdell, P. J., Franz, B.A., Bailey, S. W., Feldman, G. C., Boss, E., Brando, V. E., et al. (2013). Generalized ocean color inversion model for retrieving marine inherent optical properties. *Applied Optics*, 52, 2019–2037.
- Yentsch, C. S., & Phinney, D. A. (1997). Yellow substances in the coastal waters of the Gulf of Maine: Implications for ocean color algorithms. In S. G. Ackleson, & R. J. Frouin (Eds.), *OceanOptics XIII. Proceedings of the SPIE*, 2963. (pp. 120–131). <http://dx.doi.org/10.1117/12.266431> (<http://dx.doi.org/http://dx.doi.org/10.1117/12.266431>).
- Zibordi, G., Berthon, J.-F., Mélin, F., D'Alimonte, D., & Kaitala, S. (2009). Validation of satellite ocean color primary products at optically complex coastal sites: Northern Adriatic Sea, Northern Baltic Proper and Gulf of Finland. *Remote Sensing of Environment*, 113, 2574–2591.